Atmos. Meas. Tech., 17, 5491–5524, 2024
https://doi.org/10.5194/amt-17-5491-2024


Atmospheric Measurement Techniques
Open Access
EGU

# Independent validation of IASI/MetOp-A LMD and RAL $CH_4$ products using CAMS model, in situ profiles, and ground-based FTIR measurements

**Bart Dils[1], Minqiang Zhou[1,2], Claude Camy-Peyret[3,4], Martine De Mazière[1], Yannick Kangah[3], Bavo Langerock[1], Pascal Prunet[3], Carmine Serio[5], Richard Siddans[6], and Brian Kerridge[6]**

[1]Royal Belgian Institute for Space Aeronomy (BIRA-IASB), Brussels, Belgium
[2]Institute of Atmospheric Physics, Chinese Academy of Sciences, Beijing, China
[3]SPAce SCIence & Algorithmics (SPASCIA), Toulouse, France
[4]L'Institut Pierre-Simon Laplace (IPSL), Paris, France
[5]Scuola di Ingegneria, Università degli Studi della Basilicata (UniBas), Potenza, Italy
[6]STFC Rutherford Appleton Laboratory, Chilton, UK

**Correspondence:** Minqiang Zhou (minqiang.zhou@mail.iap.ac.cn)

Received: 9 November 2023 – Discussion started: 15 November 2023
Revised: 24 May 2024 – Accepted: 6 June 2024 – Published: 16 September 2024

**Abstract.** In this study, we carried out an independent validation of two methane retrieval algorithms using spectra from the Infrared Atmospheric Sounding Interferometer (IASI) that has been aboard the Meteorological Operational Satellite A (MetOp-A) since 2006. Both algorithms, one developed by the Laboratoire de Météorologie Dynamique (LMD), called the non-linear inference scheme (NLISv8.3), and the other by the Rutherford Appleton Laboratory (RAL), referred to as RALv2.0, provide long-term global $CH_4$ concentrations using distinctively different retrieval approaches (neural network vs. optimal estimation, respectively). They also differ with respect to the vertical range covered, where LMD provides mid-tropospheric dry-air mole fractions ($mtCH_4$), and RAL provides mixing ratio profiles from which we can derive total column-averaged dry-air mole fractions ($XCH_4$) and potentially two partial column layers ($qCH_4$).

We compared both $CH_4$ products using the Copernicus Atmospheric Monitoring Service (CAMS) model, in situ profiles (range extended using CAMS model data), and ground-based Fourier transform infrared (FTIR) remote-sensing measurements. The average difference (in $mtCH_4$) with respect to in situ profiles for LMD ranges between −0.3 and 10.9 ppb, while for RAL the $XCH_4$ difference ranges between −4.6 and −1.6 ppb. The standard deviation (SD) of the observed differences between in situ measurements and RAL retrievals is 14.1–21.9 ppb, which is consistently smaller than that between LMD retrievals and in situ measurements (15.2–30.6 ppb). By comparing with ground-based FTIR sites, the mean differences are within ±10 ppb for both RAL and LMD retrievals. However, the SD of the differences at the ground-based FTIR stations shows significantly lower values for RAL (11–15 ppb) than for LMD (about 25 ppb).

The long-term trend and seasonal cycles of $CH_4$ derived from the LMD and RAL products are further investigated and discussed. The seasonal variation in $XCH_4$ derived from RAL is consistent with the seasonal variation observed by the ground-based FTIR measurements. However, the overall 2007–2015 $XCH_4$ trend derived from RAL measurements is underestimated, if not adjusted, for an anomaly occurring on 16 May 2013 due to a L1 calibration change. For LMD, we see very good agreement at the (sub)tropics (< 35° N–35° S) but notice deviations in the seasonal cycle (both in the amplitude and phase) and an underestimation of the long-term trend with respect to the RAL and reference data at higher-latitude sites.

**Published by Copernicus Publications on behalf of the European Geosciences Union.**

## 1 Introduction

Methane ($CH_4$) is an important greenhouse gas which has a global warming potential about 28 times greater than carbon dioxide ($CO_2$) over a 100-year time horizon (IPCC, 2021). As $CH_4$ has a relatively short lifetime of about 9 years compared to $CO_2$, it is more efficient to control $CH_4$ emissions to mitigate climate change. About 60 % of atmospheric $CH_4$ is released from fossil fuels, biomass burning, landfills, and rice agriculture (anthropogenic activities) emissions, and the remaining $\sim 40$ % are coming from ruminant animals, termite, wetlands, and lake (natural) emissions (IPCC, 2021). The major sink of $CH_4$ is its reaction with the hydroxyl radical (OH) to form $CO_2$ and $H_2O$ (Rigby et al., 2017).

The globally averaged methane abundance measured by the NOAA marine surface sites shows that the dry-air mole fraction of $CH_4$ increases from 1644.65 ppb in 1984 to 1772.41 ppb in 1999, and it remains almost stable between 1999 and 2006. However, the $CH_4$ started increasing again (Rigby et al., 2008) from 1774.98 ppb in 2006 to 1911.82 ppb in 2022. Kirschke et al. (2013) showed that a rise in natural wetland and fossil fuel emissions accounts for the increase in $CH_4$ after 2006. $CH_4$ isotope measurements suggest that tropical biogenic sources are the cause of the increase (Schwietzke et al., 2016). Later, Worden et al. (2017) pointed out that there is a decrease in the biomass burning emission after 2007, and the increases from fossil fuels and biogenic sources are both important. In addition to the emissions, the variation in OH can affect the $CH_4$ mole fraction, which might also contribute to the increase after 2007 (Turner et al., 2017).

The Infrared Atmospheric Sounding Interferometer (IASI) carried aboard the Meteorological Operational Satellite A (MetOp-A) was launched to a sun-synchronous orbit on 19 October 2006 and is recording infrared spectra in the wavenumber range from 645 to 2760 $cm^{-1}$ (Edwards et al., 2006). Since then, $CH_4$ has been successfully retrieved from the IASI-observed spectra with several different algorithms, e.g. the Laboratoire de Météorologie Dynamique's (LMD) non-linear inference scheme (NLIS) (Crevoisier et al., 2009) and the Rutherford Appleton Laboratory (RAL) (Siddans et al., 2017). The LMD methane mid-tropospheric dry-air mole fraction ($mtCH_4$) has been assimilated in the Copernicus Atmosphere Monitoring Service (CAMS) greenhouse gas model (Massart et al., 2014). Note that dry-air mole fractions of methane are typically denoted as $XCH_4$ when they pertain to the total column. Therefore, in the case of LMD, or when using LMD's vertical sensitivity profile for smoothing, $mtCH_4$ is often used as a better representation of its limited vertical range. In this article, where we deal with comparisons between both total and partial column-averaged mole fractions, we sometimes refer to mere $CH_4$ but note that, depending on the products, this refers to differing dry-air mole fractions, be it $XCH_4$ (for total column RAL), $qCH_4$ (for RAL partial column), or $mtCH_4$ (for LMD or RAL smoothed by the LMD sensitivity profile; mid-tropospheric partial columns). RAL $XCH_4$ products are used for inverse modelling in order to optimize methane fluxes and to better understand the methane budget (Palmer et al., 2018). Crevoisier et al. (2013) compared the LMD data with aircraft measurements, and they found that the mean and standard deviation (SD) of the differences are within 7.2 and 16.3 ppb, respectively. Siddans et al. (2017) compared the RAL data with independent measurements from satellite, aircraft, and ground sensors and found that the precision of a single retrieval ranges from 20 to 40 ppb, and the methane ($XCH_4$) trend between 2007 and 2012 derived from the RAL product is generally consistent with the CAMS model but without a quantitative result. As both RAL and LMD IASI MetOp-A retrievals have provided a long time series of $CH_4$ observations since 2007, the two products are valuable to study the $CH_4$ trend and variation on a global scale.

In this study, we make an independent validation of LMD and RAL $CH_4$ measurements from IASI/MetOp-A using the CAMS model, aircraft and AirCore in situ profiles, and ground-based Fourier transform infrared (FTIR) measurements. The data used in this study are described in Sect. 2. The method of comparison between LMD and RAL measurements and the method of comparison between the satellite (both LMD and RAL) and reference data are discussed in Sect. 3. This section also discusses the impact of the 16 May 2013 discontinuity in the RAL data and its correction methods. Section 4 discusses internal satellite product aspects such as consistency and partial column differences (the latter only in the case of RAL). In Sect. 5, we show the results concerning the comparison between the LMD and RAL $CH_4$ measurements either directly or using CAMS as an intermediate. In Sect. 6, we compare LMD and RAL $CH_4$ with in situ and ground-based remote-sensing measurements. Discussions are carried out in Sect. 7, and conclusions are shown in Sect. 8.

## 2 Data

### 2.1 IASI satellite measurements

#### 2.1.1 RAL

The RAL retrieval algorithm is based on the optimal estimation method (OEM), described in (Rodgers, 2000), using the Levenberg–Marquardt iterative method exploiting the IASI spectra from 1232.25 to 1288.00 $cm^{-1}$. The spectral range differs from the one from IASI LMD NLISv8.3 in order to capture channels that are more sensitive to near-surface concentrations. The RAL retrievals are performed globally over land and sea by night and day (09:30 and 21:30 local solar time, LST). The retrieval scheme provides retrieved products at the IASI instantaneous field of view (IFOV) scale, selecting one of the four IFOVs within a given field of re-

gard (FOR) with the warmest brightness temperature (BT) at 950 $cm^{-1}$. This IFOV is assumed to be the one with the least amount of potential cloud contamination. The RAL retrieval scheme uses nitrous oxide ($N_2O$) spectral features in the interval to estimate effective cloud parameters (Siddans et al., 2017). The temperature, water vapour, and surface spectral emissivity are pre-retrieved from the Infrared Microwave Sounder (IMS) retrieval.

RAL data used in this study are from v2.0, covering measurement from 1 June 2007 to 31 December 2017. The RAL IASI level 2 product provides a priori and retrieved $CH_4$ profiles, a priori and retrieved column-averaged $XCH_4$ mole fractions, a column-averaging kernel, an averaging-kernel matrix, and the surface pressure. The latitude-dependent a priori $CH_4$ profile is applied. The degree of freedom for signal (DOFs) is about 2.0, with two pieces of information characterized by the partial columns of 0–6 km and 6–12 km. Note that the RAL retrievals used in this study are filtered as suggested in the RAL product user guide (Knappett, 2019). This product user guide also already identifies the bias shift on 16 May 2013 due to a L1 calibration change that was identified during the course of this analysis.

#### 2.1.2 LMD

The IASI LMD NLIS algorithm, henceforth referred to as LMD, is based on a multilayer-perceptron scheme (Crevoisier et al., 2009). The 24 IASI channels selected within the range from 1270 to 1350 $cm^{-1}$ and 2 Advanced Microwave Sounding Unit (AMSU) channels (6 and 8) are exploited to retrieve $CH_4$-integrated columns. LMD provides a vertical $CH_4$ weighting function to represent the vertical sensitivity. This product is mainly sensitive to the mid- to upper-tropospheric methane covering the vertical range between 100 and 500 hPa (Crevoisier et al., 2009, 2013). An a priori profile is not required in the LMD retrieval algorithm, and retrievals are performed over land and sea by night and day for clear-sky conditions. Clouds are detected by multispectral threshold tests using AMSU and the High resolution Infrared Radiation Sounder (HIRS/4) brightness temperature differences together with a heterogeneity test at each HIRS FOV. Initially, LMD NLIS targeted tropical regions (30° N–30° S) only. Currently, the retrievals are performed globally, with the exception of polar situations. In this analysis, for general quality markers and direct comparisons with RAL, we limit ourselves to data coming from the 60° N–60° S latitude band as advised by the product development team.

The inference scheme uses an average of the four IASI footprints contained in each single AMSU FOV. Hence, retrievals are performed at the AMSU spatial resolution, roughly comparable with the IASI field of regard composed by four IASI IFOV. The LMD data used in this study are from v8.3, covering the measurements from 1 July 2007 to 29 September 2015. LMD IASI level 2 data provide a column-averaged mole fraction and weighting function. There is no profile provided by the LMD IASI $mtCH_4$ data.

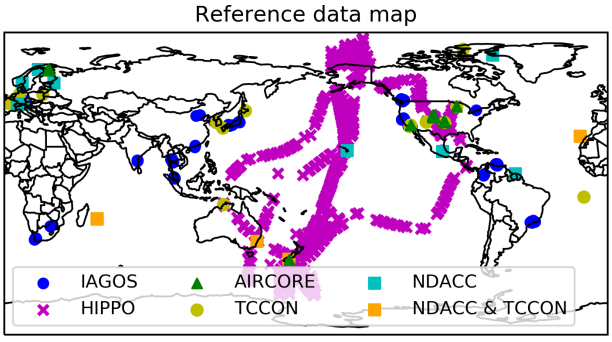


**Figure 1.** The map of the reference data used in this study, including in situ profiles and ground-based FTIR measurements.

### 2.2 In situ profiles

The geolocation of the in situ and ground-based FTIR measurements used in this study is shown in Fig. 1.

#### 2.2.1 AirCore

The AirCore is an atmospheric sampling system that uses a long tube that is carried into the stratosphere using balloons. It samples the air from the surrounding atmosphere and preserves profiles of the trace gases of interest from the surface (a few hundred metres) to the middle stratosphere (about 30 km) (Karion et al., 2010). The NOAA Global Monitoring Laboratory has carried out many AirCore launches during the last decade at selected sites (Boulder, Colorado, USA; Lamont, Oklahoma, USA; Lauder, Aotearoa / New Zealand; Sodankylä, Finland; Park Falls, Wisconsin, USA; Edwards Air Force Base, Dryden, California, USA) and more recently has made further system improvements by developing active capabilities by mounting the AirCore system on aircraft or UAV drones (Andersen et al., 2018). Here, we use the NOAA AirCore v20181101 profiles (Baier et al., 2021).

#### 2.2.2 HIPPO

The HIAPER Pole-to-Pole Observations (HIPPO) are aircraft measurements (Wofsy, 2011), using a National Science Foundation/National Center for Atmospheric Research (NSF/NCAR) Gulfstream V, performed as pole-to-pole campaigns which occurred five times during the 2009–2011 time period. The first campaign (HIPPO I) took place in January 2009, followed by HIPPO II in October–November 2009, HIPPO 3 in March–April 2010, HIPPO IV in June–July 2011, and finally HIPPO V in August–September 2011, thus covering all seasons, albeit not in the same year. HIPPO transected the mid-Pacific Ocean and returned either over the eastern or western Pacific, making frequent surface-to-tropopause ascents and descents. The HIPPO data have been

widely applied for scientific studies. Since, unlike AirCore, its vertical range does not cover the entirety of the range to which the retrieval algorithms are sensitive, we need to expand the profiles using other data (in our case, from the CAMS model, as outlined in Sect. 3.4.1).

#### 2.2.3 IAGOS

In-service Aircraft for a Global Observing System (IAGOS) is a European Research Infrastructure Consortium (ERIC) for global observations of atmospheric composition from commercial aircraft. IAGOS combines the expertise of scientific institutions with the infrastructure of civil aviation in order to provide essential data on climate change and air quality at a global scale. It is composed of two complementary systems: (i) IAGOS-CORE providing global coverage on a day-to-day basis of key observables and (ii) IAGOS-CARIBIC providing a more in-depth and complex set of observations with lesser geographical and temporal coverage. In this study, we select all the IAGOS-CARIBIC $CH_4$ profiles, measured during the ascent or descent of commercial aircraft from or towards its airport between 10 July 2007 and 31 December 2017. As with the HIPPO data, profile extension prior to the comparisons is required.

### 2.3 Ground-based FTIR measurements

#### 2.3.1 TCCON

The Total Carbon Column Observing Network (TCCON) is a network of ground-based FTIR that records spectra of the Sun in the near-infrared. From these spectra, the $CH_4$ and $O_2$ total columns are retrieved simultaneously. The retrieved windows of $CH_4$ are 5781.0–5897.0, 5996.45–6007.55, and 6007.0–6145.0 $cm^{-1}$, and the retrieved window of $O_2$ is 7765–7905 $cm^{-1}$. Since the $O_2$ volume-mixing ratio (VMR) of 0.2095 is constant in the atmosphere, TCCON uses the $O_2$ total column to calculate the total column of the dry air and then to calculate the $XCH_4$ as the ratio between the retrieved $CH_4$ total column and the total column of dry air. The advantage is that systematic errors common to the retrieval of $CH_4$ and $O_2$ retrieval partially cancel in the calculation of the column-averaged mole fractions, resulting in a high-precision data product. Furthermore, TCCON applies a calibration factor to reduce its systematic bias (Wunch et al., 2011). Currently, the TCCON network is going through a transition period while moving from the GGG2014 to the GGG2020 retrieval algorithm version. While most stations have already delivered GGG2020 data, for the time period we are analysing, many gaps are still present in the new dataset, particularly for older data that still need to be reprocessed. Instead of using a mixture of GGG2020 and GGG2014 data, we opted to use GGG2014 data exclusively. The random uncertainty in the TCCON $XCH_4$ measurement is about 0.5 % (Wunch et al., 2015). The TCCON sites used in this study are listed in Table 1.

#### 2.3.2 NDACC

The Network for the Detection of Atmospheric Composition Change (NDACC) hosts ground-based solar absorption FTIR measurements of $CH_4$ from mid-infrared spectra. NDACC uses either the SFIT4 or the PROFFIT9 algorithm to retrieve $CH_4$ vertical profiles (De Mazière et al., 2018). Good agreement between these two retrieval algorithms has been demonstrated (Hase et al., 2004), and both algorithms are based on the optimal estimation method. The $CH_4$ retrieval strategy within the NDACC community has not been fully harmonized, but it uses the $CH_4$ absorption lines around 2800 $cm^{-1}$ (3.57 µm). The DOFs is about 2.5, with about two pieces of information in the troposphere and in the stratosphere separately (Zhou et al., 2018). The systematic and random uncertainties in the NDACC $CH_4$ total column are estimated to be 3.0 % and 1.5 %, respectively. The estimated systematic uncertainty of 3.0 % is mainly coming from the uncertainty in the spectroscopy. By comparing the TCCON and NDACC $XCH_4$ measurements, Ostler et al. (2014) pointed out that there is no overall bias between TCCON and NDACC $XCH_4$ retrievals. Since the systematic uncertainty in the TCCON measurement is largely eliminated by applying a scaling factor via the comparison to in situ profiles, we can assume that there is no overall bias in the NDACC network either. For TCCON, we can estimate the accuracy of this network from the uncertainty in the scaling factor, which amounts to 0.2 %. The NDACC data provide a priori and retrieved profiles, an averaging kernel, and the surface pressure. The NDACC sites used in this study are listed in Table 2.

### 2.4 CAMS model

Given our experience with the model and our needs, the reanalysis Copernicus Atmosphere Monitoring Service (CAMS) model, a well-established European model that currently covers the 2003–2020 period, was deemed the most suitable. It comes in the form of the standard reanalysis product in which satellite methane data are assimilated (including IASI LMD NLISv8.3 and thus cannot be regarded as an independent source for quality arbitration between the two algorithms in this study) or in the form of a control run without assimilation (Inness et al., 2019). The latter one, used here, constrains the meteorological parameters by observations while the methane field is free to evolve based on transport, fluxes, and chemical loss rates (emission databases and loss rates described in Massart et al., 2014). The model provides data on a reduced Gaussian grid at a spectral truncation of T255 (which corresponds with a grid spacing of approximately 80 km). The vertical resolution consists of 60 hybrid sigma pressure levels with a top at 0.1 hPa. Note

**Table 1.** Characteristics of the TCCON sites used in this study with the location, altitude (in km a.s.l.), and reference.

| Site | Latitude | Longitude | Altitude [km] | Reference |
|---|---|---|---|---|
| Eureka | 80.05° N | 86.42° W | 0.61 | Strong et al. (2019) |
| Sodankylä | 67.37° N | 26.63° E | 0.19 | Kivi et al. (2014) |
| Białystok | 53.23° N | 23.05° E | 0.18 | Deutscher et al. (2019) |
| Bremen | 53.10° N | 8.85° E | 0.03 | Notholt et al. (2019) |
| Karlsruhe | 49.10° N | 8.44° E | 0.12 | Hase et al. (2015) |
| Orléans | 47.97° N | 2.11° E | 0.13 | Warneke et al. (2019) |
| Garmisch | 47.48° N | 11.06° E | 0.74 | Sussmann and Rettinger (2018) |
| Park Falls | 45.95° N | 90.27° W | 0.44 | Wennberg et al. (2017) |
| Rikubetsu | 43.46° N | 143.77° E | 0.38 | Morino et al. (2018b) |
| Lamont | 36.60° N | 97.49° W | 0.32 | Wennberg et al. (2016b) |
| Tsukuba | 36.05° N | 140.12° E | 0.03 | Morino et al. (2018a) |
| Edwards | 34.96° N | 117.88° W | 0.70 | Iraci et al. (2016) |
| Jet Propulsion Laboratory (JPL) | 34.20° N | 118.18° W | 0.39 | Wennberg et al. (2016a) |
| Pasadena | 34.14° N | 118.13° W | 0.23 | Wennberg et al. (2015) |
| Saga | 33.24° N | 130.29° E | 0.01 | Kawakami et al. (2014) |
| Izaña | 28.30° N | 16.50° W | 2.37 | Blumenstock et al. (2017) |
| Ascension Island | 7.92° S | 14.33° W | 0.01 | Feist et al. (2014) |
| Darwin | 12.46° S | 130.93° E | 0.04 | Griffith et al. (2014a) |
| Réunion | 20.90° S | 55.49° E | 0.09 | De Mazière et al. (2017) |
| Wollongong | 34.41° S | 150.88° E | 0.03 | Griffith et al. (2014b) |
| Lauder | 45.04° S | 169.68° E | 0.37 | Sherlock et al. (2014) |

**Table 2.** Characteristics of the NDACC sites used in this study with the location and altitude (in km a.s.l.). U. of Toronto is for the University of Toronto, Canada. NCAR is for the National Center for Atmospheric Research, USA. IMK-ASF is for the Institute of Meteorology and Climate Research – Atmospheric Trace Gases and Remote Sensing, Germany. IRF is for the Institute of Space Physics, Sweden. STEL is for the Solar Terrestrial Environment Laboratory, Nagoya University, Japan. SPBU is for the Saint Petersburg State University, Russia. KIT-IFU is for the Karlsruhe Institute of Technology – Atmospheric Environmental Research, Germany. U. Liège is for the University of Liège, Belgium. KIT-IMK is for the Karlsruhe Institute of Technology – Institute for Meteorology and Climate Research, Germany. AEMET is for the State Meteorological Agency, Spain. BIRA-IASB is for the Royal Belgian Institute for Space Aeronomy, Belgium. U. Wollongong is for the University of Wollongong, Australia. NIWA is for the National Institute of Water and Atmospheric Research, Aotearoa / New Zealand.

| Site | Latitude | Longitude | Altitude [km] | Principal investigator(s) |
|---|---|---|---|---|
| Eureka | 80.05° N | 86.42° W | 0.61 | Kimberly Strong (U. of Toronto) |
| Thule | 78.90° N | 68.77° W | 0.02 | James W. Hannigan, Ivan Ortega, Michael T. Coffey (NCAR) |
| Kiruna | 67.84° N | 20.40° E | 0.2 | Thomas Blumenstock (IMK-ASF), Uwe Raffalski (IRF), Yutaka Matsumi (STEL) |
| St Petersburg | 59.88° N | 29.83° E | 0.02 | Maria Makarova (SPBU) |
| Garmisch | 47.48° N | 11.06° E | 0.74 | Ralf Sussmann (KIT-IFU) |
| Zugspitze | 47.42° N | 10.98° E | 2.96 | Ralf Sussmann (KIT-IFU) |
| Jungfraujoch | 46.55° N | 7.98° E | 3.58 | Emmanuel Mahieu (U. Liège) |
| Izaña | 28.30° N | 16.50° W | 2.37 | Matthias Schneider (KIT-IMK), Omaira Garcia (AEMET) |
| Mauna Loa | 19.54° N | 155.57° W | 3.40 | James W. Hannigan, Ivan Ortega, Michael T. Coffey (NCAR) |
| Réunion Saint-Denis | 20.90° S | 55.49° E | 0.09 | Martine De Mazière (BIRA-IASB) |
| Réunion Maïdo | 21.08° S | 55.38° E | 2.16 | Martine De Mazière (BIRA-IASB) |
| Wollongong | 34.41° S | 150.88° E | 0.03 | Nicholas Jones, David Griffith (U. Wollongong) |
| Lauder | 45.04° S | 169.68° E | 0.37 | Dan Smale, John Robinson (NIWA) |

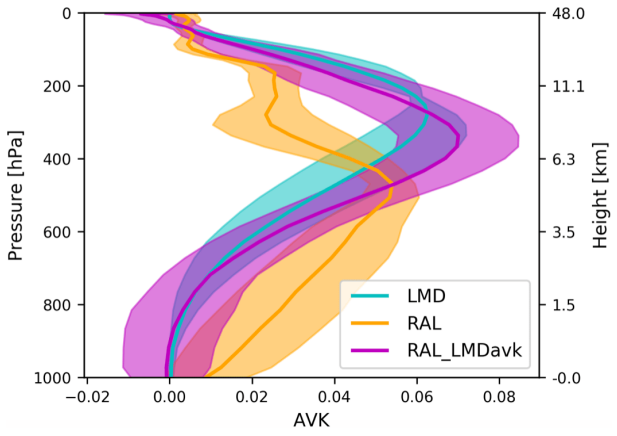


**Figure 2.** The vertical sensitivities of LMD, RAL, and RAL smoothed with the column-averaging kernel of LMD (RAL_LMDavk). The solid line is the global annual mean in 2014, and the shadow is the standard deviation of all the averaging kernels in 2014.

that prior to our analysis, we regridded the model output onto a $1^\circ \times 1^\circ$ latitude–longitude regular horizontal grid. More information about the CAMS reanalysis greenhouse model is available at https://confluence.ecmwf.int/display/CKB/CAMS%3A+Reanalysis+data+documentation (last access: 12 January 2023) and Agusti-Panareda et al. (2017).

The performance of the CAMS reanalysis $XCH_4$ control run in the 2003–2016 period has been validated using (among others) ground-based FTIR measurements (Ramonet et al., 2020), and it is found that the mean differences between the CAMS model and FTIR measurements are −0.7 % in the troposphere and 3.6 % in the stratosphere. The CAMS model can well capture the long-term trend in $XCH_4$ between 2003 and 2016. For the column-averaged mole fraction, the average biases at individual stations always remained below 20 ppb, with slightly higher CAMS values over mid- and high latitudes and lower values in the tropics with respect to the FTIR measurements.

## 3 Method

### 3.1 Smoothing RAL profile with LMD weighting function

To compare LMD with the RAL $CH_4$ measurements, we need to take the vertical sensitivity into account (Rodgers and Connor, 2003). Figure 2 shows the vertical sensitivities of both the LMD- and RAL-retrieved $CH_4$. While the LMD retrieval is mainly sensitive to the mid- to upper troposphere, RAL's sensitivity extends to lower altitudes.

For the LMD retrieval, the $mtCH_4$ product can be written as follows:

$$c_{\mathrm{r,L}} = \frac{\boldsymbol{w} \cdot \mathrm{dp} \cdot \boldsymbol{x}_t}{\sum \boldsymbol{w} \cdot \mathrm{dp}} = \mathbf{A}_{\mathrm{L}} \cdot \boldsymbol{x}_t + \epsilon_L, \quad (1)$$

where $c_{\mathrm{r,L}}$ is the retrieved LMD $mtCH_4$ and $\epsilon_L$ the retrieval errors without the smoothing effects. $\boldsymbol{w}$ is the weighting function of the LMD retrieval interpolated on a pressure grid of thickness dp, $\boldsymbol{x}_t$ is the true $CH_4$ profile, and $\mathbf{A}_{\mathrm{L}}$ is the resulted weighting function on the new grid.

For the RAL retrieval,

$$\boldsymbol{x}_{\mathrm{r,R}} = \boldsymbol{x}_{\mathrm{a}} + \mathbf{A}_{\mathrm{R}}(\boldsymbol{x}_t - \boldsymbol{x}_{\mathrm{a}}) + \epsilon_R, \quad (2)$$

where $\boldsymbol{x}_{\mathrm{r,R}}$ and $\boldsymbol{x}_{\mathrm{a}}$ are the retrieved and a priori $CH_4$ profiles. $\mathbf{A}_{\mathrm{R}}$ is the averaging-kernel matrix and $\epsilon_R$ the retrieval errors without the smoothing effects.

In this study, when we directly compare LMD to RAL, we calculated, from the RAL profile, the mid-tropospheric column-averaged $mtCH_4$, named RAL_LMDavk, using the LMD weighting function as follows:

$$\boldsymbol{x}_{\mathrm{RAL\_LMDavk}} = \frac{\boldsymbol{w} \cdot \mathrm{dp} \cdot \boldsymbol{x}_{\mathrm{r,R}}}{\sum \boldsymbol{w} \cdot \mathrm{dp}}. \quad (3)$$

The vertical sensitivity of the RAL_LMDavk is also shown in Fig. 2, which becomes much closer to that of the LMD retrieval. Then, the difference between LMD and RAL_LMDavk retrievals is mainly coming from the smoothing error in the RAL retrieval smoothed with the vertical sensitivity of the LMD retrieval.

### 3.2 Comparison with the CAMS model

Prior to comparing RAL and LMD $CH_4$ with CAMS model data, all data, including averaging kernels and sensitivities, are averaged onto a $1^\circ \times 1^\circ$ latitude–longitude grid. Satellite data are divided into day- and nighttime data based on the solar zenith angle. We then construct a single daily daytime and nighttime CAMS global field by selecting from the standard 3 h output those longitude bands that most closely correspond with the local IASI daytime (09:30 LST) and nighttime (21:30 LST) overpass times. Subsequently, the daytime/nighttime model data are interpolated onto the satellite's vertical grid, and smoothing is applied as per Sect. 3.1. This allows a straightforward comparison between the satellite and model global fields. In the case of comparisons with RAL_LMDavk, the CAMS data are first subject to smoothing using the RAL profile averaging kernel, after which we apply the LMD vertical sensitivity.

### 3.3 Co-located data pair between satellite and reference measurements

For each in situ profile (aircraft or AirCore), we use the same spatiotemporal criteria to select the co-located RAL and LMD satellite footprints. The IASI-retrieved values (also called satellite measurements or satellite values for simplicity) are selected within a temporal window of ±6 h and a spatial distance within ±1.0° latitude and ±3.0° longitude. Then, the mean of the satellite values is applied to compare with the in situ measurement. The number of individual RAL

satellite data points that are typically averaged ranges between 1 and 24, with a mean of 8.1 measurements. The SD of the RAL co-located $XCH_4$ is about 12.4 ppb. For LMD, the number of averaged data points ranges between 1 and 15, with a mean of 3.9 measurements. The SD of the LMD co-located $mtCH_4$ is about 9.1 ppb.

For the ground-based FTIR measurement, we also use the mean of the co-located satellite measurements to compare with each individual FTIR measurement. Several spatiotemporal criteria have been tested, and the following spatiotemporal criteria are finally set to select the co-located satellite footprints. Note that the criteria are different with TCCON or NDACC and LMD or RAL, which is mainly due to the different data densities of both ground-based FTIR and satellite measurements.

- *RAL vs. TCCON*.
  Co-located criteria: ±1 h and within a ±0.5° latitude and ±1.5° longitude.
- *RAL vs. NDACC*.
  Co-located criteria: ±3 h and within a ±0.5° latitude and ±1.5° longitude.
- *LMD vs. TCCON*.
  Co-located criteria: ±1 h and within a ±1.0° latitude and ±3.0° longitude.
- *LMD vs. NDACC*.
  Co-located criteria: ±3 h and within a ±1.0° latitude and ±3.0° longitude.

As always, these criteria are a compromise between the need to gather enough data pairs to facilitate the statistical analysis at the cost of introducing additional co-location biases. The sparseness of data at certain reference sites, as well as our focus on large-scale phenomena (long-term trends and large-region biases) and the fact that the near-surface sensitivity of IASI is limited (and thus less influenced by local emissions), prompted us to adopt the above co-location criteria.

### 3.4 Comparison with reference data

#### 3.4.1 Satellite vs. in situ measurements

According to Rodgers and Connor (2003), the vertical sensitivity of the remote-sensing data should be taken into account when comparing to the in situ profile. To that end, we need to extrapolate the in situ profile to the whole atmosphere as the vertical coverage of the in situ profile (IAGOS, HIPPO, and, to a lesser extent, AirCore) is limited. In this study, we use the CAMS model to extend the in situ profile. For the vertical range above the maximum height of the in situ data, we use the CAMS model profile but scaled with altitude-dependent factors. The scaling factor is equal to 1 at the top of the atmosphere and to the mean ratio of the CAMS model to the in situ measurements at the highest three levels where the CAMS profile meets up with the top of the measured profile. A linear fitting is applied to create the scaling factors between the maximum height of the in situ profile and the top of the atmosphere. For the vertical range below the minimum height of the in situ profile, the CAMS model with a constant offset is used. The offset is calculated as the mean difference between the CAMS model and in situ data in the lowest three levels. Of the three datasets, only AirCore measures well into the stratosphere, capturing the sharp $CH_4$ decreases as one goes from the troposphere into the stratosphere. Therefore, any observed differences between the validation results are at least in part due to inaccuracies within the extrapolated, scaled model part of the in situ profiles, certainly in light of the differing vertical sensitivities between RAL and LMD. Other factors are differences in geographical coverage, with HIPPO covering the Pacific region, IAGOS restricted to a handful of international airports, and AirCore limited to a few sites in the United States, Aotearoa / New Zealand (Lauder), and Finland (Sodankylä) (see Fig. 1).

- *RAL against in situ profile*.
  The smoothed $XCH_4$ in situ measurement $c_i$ is calculated as follows:

$$c_i = c_a + \boldsymbol{a}_S(\boldsymbol{x}_i - \boldsymbol{x}_a), \tag{4}$$

  where $\boldsymbol{a}_S$ is the RAL column-averaging kernel vector, $\boldsymbol{x}_a$ and $\boldsymbol{x}_i$ are the RAL a priori profile and in situ profile, respectively, and $c_a$ is the RAL IASI a priori $XCH_4$.

  For profile comparison, we also calculate the smoothed $CH_4$ profile in situ measurement $\boldsymbol{x}'_i$ as follows:

$$\boldsymbol{x}'_i = \boldsymbol{x}_a + \mathbf{A}_R(\boldsymbol{x}_i - \boldsymbol{x}_a), \tag{5}$$

  using RAL's $\mathbf{A}_R$ averaging-kernel matrix.

- *LMD against in situ profile*.
  LMD IASI data only provide $mtCH_4$ together with the weighting function $\boldsymbol{w}$. There is no information about the a priori profile and the surface pressure.

$$c_i = \frac{\boldsymbol{w} \cdot \mathrm{dp} \cdot \boldsymbol{x}_i}{\sum \boldsymbol{w} \cdot \mathrm{dp}} \tag{6}$$

#### 3.4.2 Satellite vs. FTIR measurements

When comparing the satellite and ground-based FTIR measurements, we need to take both the a priori profile and vertical sensitivity into account.

- *RAL against TCCON measurements*.
  TCCON and RAL IASI data both provide their respective a priori profiles. Here, we use the TCCON a priori profile as the common a priori profile to adapt the RAL IASI data.

$$c'_{r,R} = c_{r,R} + c_{a,T} - c_{a,R} + \boldsymbol{a}_S(\boldsymbol{x}_{a,R} - \boldsymbol{x}_{a,T}), \tag{7}$$

where $c_{r,R}$ is the original RAL $XCH_4$ data, $\boldsymbol{a}_S$ is the RAL column-averaging kernel vector, $\boldsymbol{x}_{a,R}$ and $\boldsymbol{x}_{a,T}$ are the RAL and TCCON a priori profiles, and $c_{a,R}$ and $c_{a,T}$ are the RAL and TCCON a priori $XCH_4$, respectively. $c'_{r,R}$ thus corresponds with the RAL $XCH_4$, where its original a priori has been replaced by TCCON's a priori profile (Rodgers and Connor, 2003).

To take the vertical sensitivity of the RAL retrieval into account, we apply the smoothing correction on the retrieved FTIR profile. However, TCCON only delivers a total column-averaged mole fraction and no retrieved profile on which we could apply our sensitivity corrections. This is due to the fact that TCCON performs a scaling profile retrieval that does not allow for variation in the profile shape. In this study, we calculate the ratio of the TCCON-retrieved $XCH_4$ ($c_{r,T}$) to the a priori $XCH_4$ ($c_{a,T}$), and the ratio is then multiplied by the TCCON a priori profile $\boldsymbol{x}_{a,T}$ as the retrieved TCCON profile ($\boldsymbol{x}_{r,T}$). After that, we apply the smoothing correction using the RAL IASI column-averaging kernel,

$$c'_{r,T} = c_{a,T} + \boldsymbol{a}_S(\boldsymbol{x}_{r,T} - \boldsymbol{x}_{a,T}), \tag{8}$$

where $c'_{r,T}$ is the adapted TCCON $XCH_4$. The $\boldsymbol{x}_{r,T}$ is regridded to the RAL retrieval grid so that the $c'_{r,T}$ and $c'_{r,R}$ have been computed on the same vertical layers.

Here, we compare $c'_{r,T}$ with $c'_{r,R}$.

– *RAL against NDACC measurements*.
NDACC and RAL IASI data both provide the a priori profiles, and we apply the NDACC a priori profile as the common a priori profile to adapt the RAL–IASI-retrieved $CH_4$ profile.

$$c''_{r,R} = c_{r,R} + c_{a,N} - c_{a,R} + \boldsymbol{a}_S(\boldsymbol{x}_{a,R} - \boldsymbol{x}_{a,N}), \tag{9}$$

where $c_{a,N}$ is the NDACC a priori $XCH_4$, and $\boldsymbol{x}_{a,N}$ is the NDACC a priori $CH_4$ profile. $c''_{r,R}$ thus corresponds with the RAL $XCH_4$, where its original a priori has been replaced by NDACC's a priori profile.

The retrieved NDACC $CH_4$ profile ($\boldsymbol{x}_{r,N}$) is smoothed with the RAL IASI column-averaging kernel to consider the vertical sensitivity of the RAL IASI data.

$$c'_{r,N} = c_{a,N} + \boldsymbol{a}_S(\boldsymbol{x}_{r,N} - \boldsymbol{x}_{a,N}), \tag{10}$$

where $c'_{r,N}$ is the adapted NDACC $XCH_4$. The $\boldsymbol{x}_{r,N}$ is regridded to the RAL retrieval grid, so that the $c'_{r,N}$ and $c''_{r,R}$ have the same vertical ranges.

Here, we compare $c'_{r,N}$ with $c''_{r,R}$.

– *LMD against TCCON measurements*.
LMD IASI data only provide $mtCH_4$, together with the weighting function $\boldsymbol{w}$. LMD does not provide an a priori profile so that it is not possible to apply a priori substitution as for RAL (see Eqs. 7 and 9).

The LMD weighting function $\boldsymbol{w}$ is thus directly applied onto the scaled TCCON a priori profile $x_{r,T}$, which is used as a proxy for a TCCON-retrieved profile. By doing this, we can not only include the vertical sensitivity of the LMD retrieval but also reduce the uncertainty resulting from the TCCON near-surface profile shape since the LMD weighting function is equal to 0 in the lower troposphere.

$$c''_{r,T} = \frac{\boldsymbol{w} \cdot \mathrm{dp} \cdot \boldsymbol{x}_{r,T}}{\sum \boldsymbol{w} \cdot \mathrm{dp}} \tag{11}$$

Here, we compare the LMD data $c''_{r,T}$ with $c_{r,L}$.

– *LMD against NDACC measurements*.
Similarly, we applied the LMD IASI weighting function $\boldsymbol{w}$ onto the retrieved NDACC $CH_4$ profile.

$$c''_{r,N} = \frac{\boldsymbol{w} \cdot \mathrm{dp} \cdot \boldsymbol{x}_{r,N}}{\sum \boldsymbol{w} \cdot \mathrm{dp}} \tag{12}$$

Here, we compare the LMD data $c''_{r,N}$ with $c_{r,L}$.

### 3.5 Measurement uncertainty

The uncertainty in each in situ profile is carefully estimated. For the vertical range within the in situ measurements, the uncertainty is from the reported measurements, with 1.3 ppb for IAGOS data (Filges et al., 2015), 1.5 ppb for AirCore data (Karion et al., 2010), and 1.5 ppb for HIPPO data (Wunch et al., 2010). For the vertical range above the in situ measurements, we use the difference between the model and the scaled model as the uncertainty. For the vertical range below the in situ measurements, the mean difference between the model and in situ measurement in the troposphere (below $\sim$ 150 hPa) is used as the uncertainty.

The combined uncertainty from satellite and in situ measurements is calculated as

$$\sigma_c = \sqrt{\sigma_{sat}^2 + \sigma_i^2}, \tag{13}$$

where $\sigma_{sat}$ is the uncertainty in satellite data, and $\sigma_i$ is the uncertainty in the in situ measurements. For the RAL measurement, the uncertainty is reported in the public data (about 35 ppb). For the LMD measurement, since there is no uncertainty value available, the SD of the co-located satellite data is used as the uncertainty. Note that we only select the FTIR and satellite data pair with more than two co-located satellite footprints.

### 3.6 Trend and seasonal variation

In this study, we derive the trend and seasonal variation in $CH_4$ between 1 July 2007 and 30 June 2015 (8 full years) from LMD and RAL measurements. We limit ourselves to this period to make sure the two satellite datasets have the same time coverage. According to the NOAA surface

measurements (Dlugokencky et al., 1994), the global $CH_4$ mean concentration kept increasing between July 2007 and June 2015 with an annual growth rate of $6.9 \pm 0.6$ ppb yr$^{-1}$ (WMO, 2017).

The level 2 satellite data are binned into $1° \times 1°$ grids to generate the level 3 daily means. The monthly data are created based on the daily data, and then the long-term trends and seasonal variations are calculated from the monthly means at each grid. To derive the trends from the month means $\boldsymbol{Y}(t)$ with $t$ the time in a fractional year, we use a regression model that includes a periodic function to describe the seasonal cycle as follows:

$$\begin{aligned}\boldsymbol{Y}(t) =& A_0 + A_1\boldsymbol{t} \\ &+ \sum_{k=1}^{3}(A_{2k}\cos(2k\pi\boldsymbol{t}) + A_{2k+1}\sin(2k\pi\boldsymbol{t})),\end{aligned} \tag{14}$$

where $t$ is in fraction of year, $A_0$ is the intercept, $A_1$ is the annual trend, and $A_2$ to $A_7$ are the periodic amplitudes. Then, the de-trended data ($\boldsymbol{Y}(t)_\mathrm{d}$) are calculated as

$$\boldsymbol{Y}(t)_\mathrm{d} = \boldsymbol{Y}(t) - (A_0 + A_1 \cdot \boldsymbol{t}). \tag{15}$$

The seasonal variation is represented by the monthly means of the de-trended data and their associated uncertainty ($2\sigma$).

### 3.7 The discontinuity in RAL data after 16 May 2013

Figure 3 shows the temporal evolution of all daily averaged data between 60° N and 60° S (left) and the prior-to post-day differences (right) for RAL total column (first row), RAL smoothed by the LMD sensitivity profile (second row), RAL's upper (6–12 km) partial column (third row), and RAL's lower (0–6 km) partial column (fourth row). It clearly shows that, due to a change in the processing of the spectral response model on 16 May 2013, a $6.7 \pm 1.5$ ppb discontinuity occurred in RAL's retrieved total column methane (top). This issue has been reported in the RAL product user guide (https://catalogue.ceda.ac.uk/uuid/f717a8ea622f495397f4e76f777349d1, last access: 12 January 2023). Note that no such effect is visible in the LMD data (not shown), nor can we clearly distinguish a discontinuity in RAL's mid-tropospheric mt$CH_4$ concentrations, obtained by smoothing the RAL profiles with the LMD sensitivity profile, from the overall variability in the data (Fig. 3; second row). It is found that this issue effects the RAL's lower partial columns (0–6 km by $\sim 9.6 \pm 2.2$ ppb) to a greater extent than the higher layers (6–12 km by $\sim 3.6 \pm 1.1$ ppb), which might explain the more limited impact on the LMD smoothed RAL profiles. The above values were determined by taking, for each day, the median $CH_4$ concentration between 60° N and 60° S. From this we calculated the difference between the median concentration value prior to and after the day in question and determined the value that corresponded with the 16 May 2013 transition (the difference between the median concentration on the 17 and 15 May). In all cases, apart from RAL's LMD smoothed mt$CH_4$ ($0.2 \pm 2.7$ ppb), this is the most prominent feature in the day-to-day variability plot (Fig. 3 (right)). As an indicator of the uncertainty, we took the standard deviation of all these day-to-day difference values 1.5 months prior to and after the transition. Note that we take on a single correction factor only – without a latitudinal or seasonal dependency. This was investigated, and differences do appear, but when taking their (considerable) uncertainties into account, none of the data subset correction factors showed a deviation from the general 60° N–60° S correction, described above, that was statistically significant.

As such, this issue complicates our analysis, and depending on the quality parameters we wanted to explore, we have either focused on a particular year, applied a simple +6.7 ppb correction on RAL's post-16-May-2013 $XCH_4$ total column concentrations (+9.6 and +3.6 ppb in case of RAL q$CH_4$ partial columns) or have regarded the pre- and post-16-May-2013 RAL measurements as two independent datasets, after which the quality parameters are averaged, using the covered time frames as weights. The latter method has the advantage of not having to add a correction parameter which adds additional uncertainty. On the downside, cutting the time series in two leaves us with a relatively short 3-year (2013–2016) time period, resulting in significantly more uncertainty in the obtained statistical parameters when the data density is low. Therefore, unfortunately, since regarding the RAL data as two independent datasets may often be considered the best solution, the limited data density of the reference measurements at many sites, and the fact that the then obtained parameters would greatly depend on the temporal range of the reference measurement, prompts us to primarily use a post-16-May bias shift. We have indicated in each case what (if any) correction method has been used. The potential impact of each of these correction methods is further discussed in Sect. 5.2.

## 4 Product analysis

In this section, prior to our RAL–LMD intercomparisons and validation with reference data, we looked at several parameters within each of the datasets. In particular, we were interested in the internal consistency of the day–night, scan angle, residual cloud cover, and IFOV-to-IFOV differences. The latter is done for RAL only as this information is not present in the LMD product, which takes the average of the four IFOVs within a FOR. This was done by drawing up histogram plots and looking at the distribution of the global data (not shown here) for the month of October 2014. We also specifically looked at RAL's partial column differences.

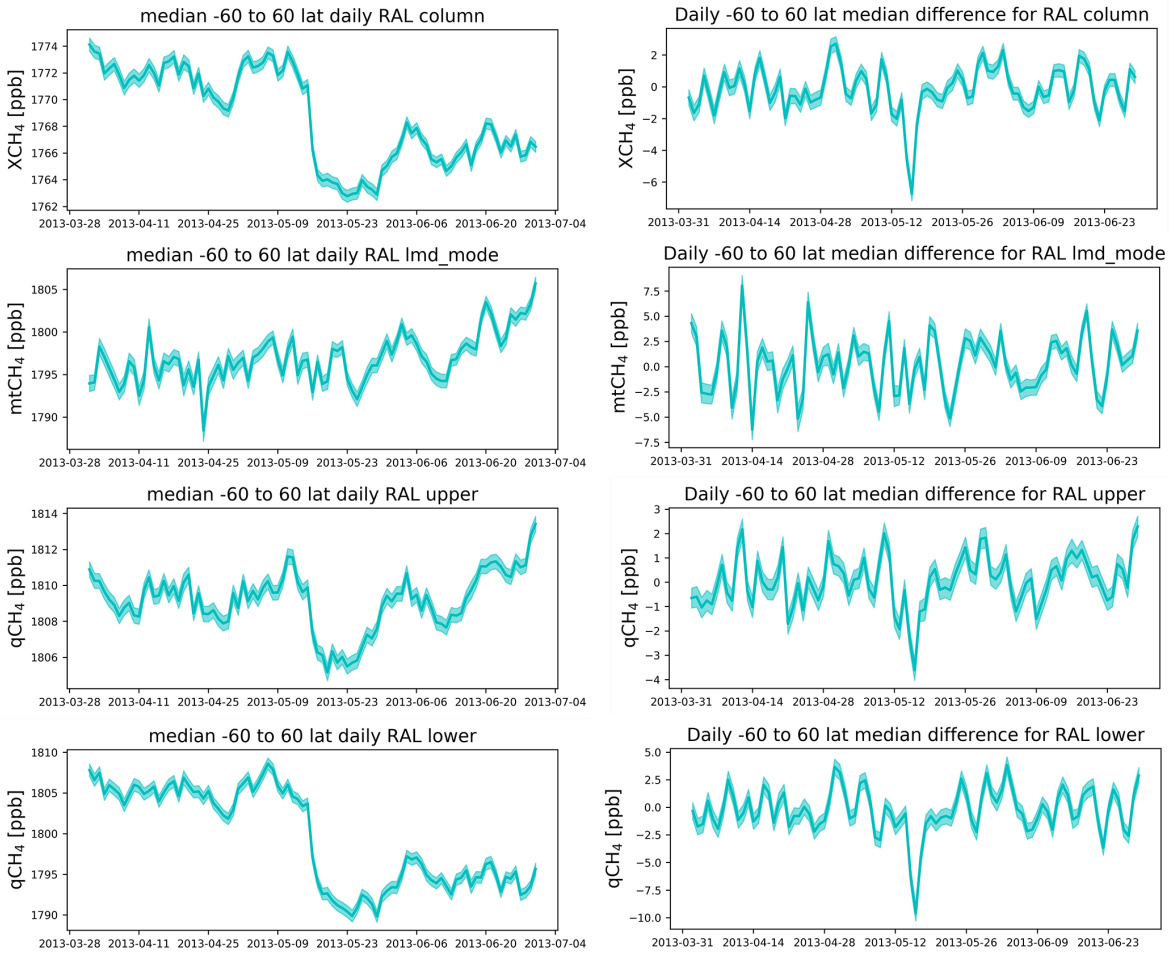


**Figure 3.** Left: evolution of the median $CH_4$ concentration around 16 May 2013 for the −60° to 60° latitude band for RAL $XCH_4$ (top), RAL_LMDavk $mtCH_4$ (second row), RAL (6–12 km) $qCH_4$ (third row), and RAL (0–6 km) $qCH_4$ (last row). Right: the difference between the median −60° to 60° concentrations before and after a given date for RAL $XCH_4$ (top), RAL_LMDavk $mtCH_4$ (second row), RAL (6–12 km) $qCH_4$ (third row), and RAL (0–6 km) $qCH_4$ (last row).

### 4.1 Internal consistency

For $mtCH_4$ LMD, we observed very small day–night differences in the distribution over land, with a slightly lower mean (∼ 4 ppb) for daytime data compared to nighttime data. Also, $mtCH_4$ values are slightly higher (∼ 7 ppb) for the edge-viewing angles than for the nadir measurements.

For $XCH_4$ RAL, we observe slight day–night differences (within 5 ppb) in the averaged distribution. The day uncertainties (typical SD of ∼ 15–20 ppb) are, as expected, lower than night uncertainties (typical SD of ∼ 35–40 ppb). Also, its nadir values are higher (up to 11 ppb) than its edge-viewing angle data on the monthly and global mean $XCH_4$, especially over sea. Also, the nadir measurements exhibit lower retrieval uncertainties (∼ 5 ppb over land/day on the median of the global distributions). Concerning the inter-IFOV differences, the highest differences are observed for daytime $XCH_4$ and between IFOV 3 and IFOV 1, with averaged differences of about 7 ppb over land and 8 ppb over sea. The inter-IFOV retrieval uncertainties are all within 3 ppb. This difference is unexpectedly large and should be further investigated at the L1 data-processing level. However, since this kind of inter-IFOV analysis that focuses on radiometric biases is not available in the IASI public reports, we were not able to derive a clear instrumental effect explaining the IFOV 1–IFOV 3 relative departure. Also, filtering with the IASI L2 cloud fraction had a slight impact (about 3 ppb on average) on the global distribution for the $XCH_4$. There is a slight decrease in the retrieval errors of about 2 ppb on average for the cloud fraction < 15 %. All this indicates that the RAL cloud-filtering condition already eliminates most of cloud-affected scenes.

The above analysis does not exclude stronger differences on a regional scale. For instance, strong negative day–night (with higher nighttime values) differences can be observed over desert regions (see Fig. 4) in both LMD and RAL. Sur-

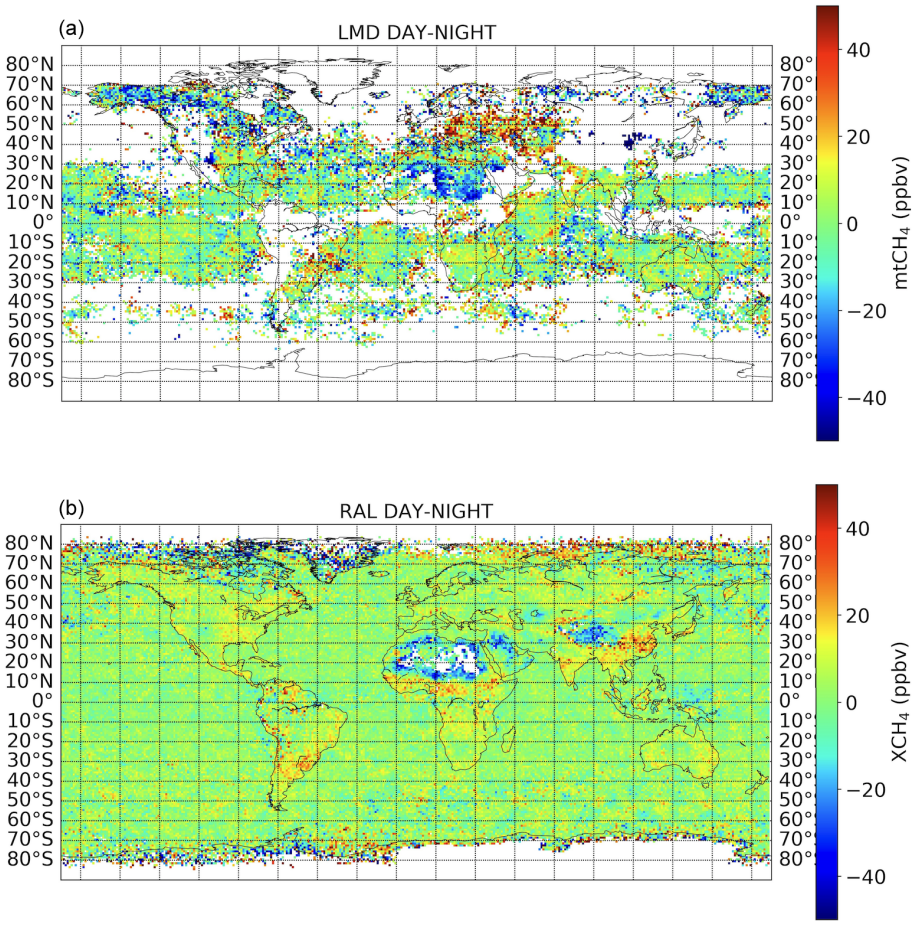


**Figure 4.** Monthly averaged LMD day–night $mtCH_4$ **(a)** and column-averaged RAL **(b)** day–night $XCH_4$ differences for April 2012.

face emissivity is difficult to handle in some areas of the Sahara where it is particularly low. This typically causes a negative difference, which is larger in the day than at night due to the high surface–air temperature contrast. Likewise, high surface–air temperature contrasts can trigger the elevation of surface emissions and can thus induce a positive day–night difference. Note that all biases are present with differences in seasonal variations and in various regions, and spectral and angular dependencies vary between different land types and surface topologies, respectively, in different areas.

### 4.2 RAL partial columns

The DOFs of RAL indicate that, apart from the higher latitudes ($> 60°$ north and south), two independent partial columns can be obtained from the retrieved profiles. Therefore, in this section, we calculate for both RAL and the smoothed CAMS profiles the monthly averaged partial columns between 0–6 km (lower layer) and 6–12 km (upper layer) for all years. In Fig. 5, we show 2012 as an example year to compare RAL with the CAMS model. Small interannual absolute value differences do occur, but the observations and conclusions discussed below remain the same. We also need to point out that the RAL product comes with a 50-layer column-averaging kernel, but the profile averaging kernel is a $5 \times 50$ matrix, where the smallest dimension corresponds with the lowest 5 levels of a coarser 12-level retrieval pressure grid. The three lowest levels of this lower resolution grid correspond with 1000, 422, and 178 hPa, respectively. The latter two pressure levels correspond with the limits of the 0–6 and 6–12 km altitude range of the partial columns. While these pressure ranges roughly contain 1 DOFs each, one cannot specifically select, due to the low-resolution grid, the partial column vertical range based on the DOFs for each measurement, and therefore, we cannot state that these column layers are fully independent in all cases.

Figure 5 shows the differences between RAL and CAMS $qCH_4$ values in the upper and lower layers in January, April, July, and October 2012. The mean and SD of the differences are only calculated for the low- and mid-latitude regions ($< 60°$ north and south). It is apparent that the $qCH_4$ observed by RAL is generally 3.1–8.0 ppb larger than the CAMS model in the upper layer and 5.5–7.7 ppb lower than the CAMS model in the lower layer. Specifically, the RAL

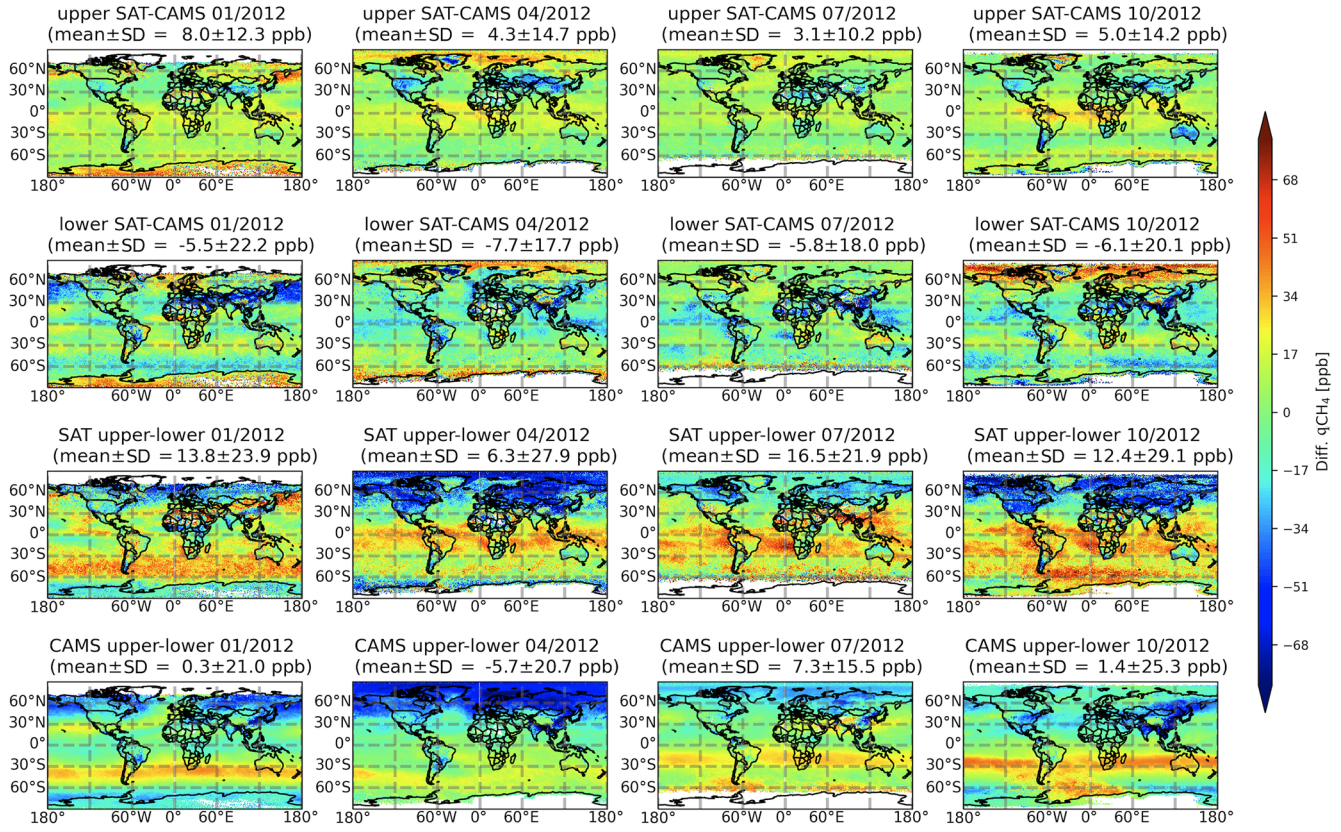


**Figure 5.** The difference in the $qCH_4$ in the upper layer (first row) and the lower layer (second row) between the RAL (SAT) and CAMS. Besides, the differences between the upper $qCH_4$ and lower $qCH_4$ are derived from RAL (third row) and CAMS (last row) in January, April, July, and October 2012.

$qCH_4$ in the lower layer is generally lower than the CAMS model in the Mediterranean area, tropics, East Asia, and South America, depending on the month of the year. The mean underestimation in the Pacific Ocean between 15° N and 15° S during these 4 months is 12.5 ppb smaller than the CAMS model.

Based on the SD of the differences, the spatial variability between the RAL and CAMS $qCH_4$ in the upper layer is less than that in the lower layer. The difference in $qCH_4$ between the upper and lower layers from RAL and CAMS is also shown in Fig. 5. For RAL, the mean upper–lower difference ranges between 6.3 and 16.5 ppb, while for CAMS the difference ranges between −5.7 and 7.3 ppb. For CAMS, in most conditions, the difference between the upper and lower $qCH_4$ is either very small or the lower layer yields higher concentrations than the upper layer. A notable exception is the band of positive (upper–lower) bias values located around the Southern Hemisphere subtropics, which is more pronounced in summer than in winter. This latitudinal structure is equally captured by RAL, but the difference between upper and lower $qCH_4$ is far more pronounced in a far wider region throughout the whole year, with peaks in summer and autumn. Note that none of these features is inherent to the RAL a priori, which exhibits a uniform near-zero partial column bias, apart from the polar regions, where the lower partial column is $\sim$ 25 ppb higher than the upper partial column, and this probably stems from the lack of sufficient spectral information.

Also apparent is the often stark contrast between adjacent land and sea measurements. Some striking examples of this situation are Australia in October and northern Europe in April. These features are not replicated in the CAMS partial column biases, which show (as expected) a smooth transition from land to sea even though the relevant averaging-kernel smoothing has been applied. While we expect differences in sensitivity to occur between land and sea measurements (a change in the retrieval uncertainty and with that the DOFs is expected), ideally the impact thereof is translated into the averaging kernel. Note that these features are not clearly present in the LMD and RAL total column product.

### 4.3 Short summary

While most parameters investigated point to no major issues (i.e. day–night differences over the Sahara desert can be readily explained), RAL's inter-IFOV bias prompts further investigation. The upper–lower $qCH_4$ partial column difference is

consistent with that observed by CAMS, but here again, the difference between adjacent land and sea partial column differences requires further investigation. Other points where RAL differs significantly from CAMS include the far more pronounced (in magnitude and time) band of positive (upper-lower) bias values located around the Southern Hemisphere subtropics.

## 5 Direct intercomparison

In order to directly compare RAL with LMD retrievals, we need to consider some inherent differences between the satellite products first. Foremost, and already discussed, are the differing sensitivities as a function of altitude. Another source of differences is that RAL selects a single IFOV with the warmest brightness temperature among the four of them within any given IASI FOR, whereas LMD uses a combination thereof, so a direct comparison on a measurement-by-measurement basis is impossible. Instead, we opted to use the CAMS model as an intermediate. Not only can we compare the gridded satellite products to the model and to one another, but we can also compare their respective biases towards the model. Doing so overcomes, to a great extent, the fact that even when looking at the bias between LMD and RAL_LMDavk mt$CH_4$, differences in vertical sensitivity remain. We should also point out at this stage that the model data are no substitute for reality and that they can harbour errors of their own. Of particular concern, particularly with respect to comparisons with the LMD data as they are more sensitive at higher altitudes, is the accuracy of the location of the upper troposphere–lower stratosphere (UTLS) transition zone within the model.

### 5.1 Absolute differences

Figure 6 shows the monthly mean global bias (for January, April, July, and October 2012) between the satellite products and the CAMS model, whereby the model is always smoothed with the respective sensitivity or averaging-kernel profile. This is done for both LMD (top row), RAL (second row), and RAL smoothed by the LMD sensitivity profile (third row). As one can see, all products have their distinct regional and seasonal biases with respect to CAMS. All products seem to feature stronger biases at high latitudes, with LMD featuring particularly strong negative biases around the month of October in the northern boreal regions and RAL (total column and LMD smoothed) featuring strong positive values compared to CAMS (particularly over northern latitudes in April and over Antarctica in January, with RAL inland Greenland being a curious exemption to this pattern). To limit the impact of these regions, the overall monthly mean biases as shown in the figure are drawn up from all values within 60° north and south, in line with LMD's recommended latitude range. We also found a few cases in which the application of the RAL column-averaging kernel onto the CAMS profile yielded clear erroneous outliers. These have been filtered out using an interquartile distance filter. No more that five measurements needed to be removed for each month. Looking at the thus obtained values, we see that the RAL column-averaged product features the lowest bias with respect to CAMS and with lower scatter than LMD. The overall bias between RAL_LMDavk and CAMS, on the other hand, is very similar to that of LMD–CAMS. Its scatter (SD of the RAL_LMDavk–CAMS differences) is similar to that of total column RAL.

The bottom two rows in Fig. 6 feature the comparison between LMD and RAL_LMDavk (fourth row) and, finally, the difference in the respective biases of LMD and RAL_LMDavk with respect to CAMS (bottom row). This last comparison should, in theory, have minimized most of the residual sensitivity differences between both products and is thus the most accurate representation of their respective overall differences. The direct comparison between LMD and RAL_LMDavk (fourth row) still yields overall negative bias values in excess of $-10$ ppb. This disappears to a large extent when looking at their respective biases towards CAMS (bottom row), indicating that even when smoothing RAL with the LMD sensitivity profile, their inherent sensitivity differences remain substantial. This observation is important when interpreting further comparison results. Also, while the average bias is small, we can still observe significant regional and seasonal biases between the products. To highlight just a few areas, in January we observe large positive LMD–RAL bias values over the Pacific between 10 and 30° N, as well as more moderate positive biases over the entire northern hemispheric Atlantic Ocean and western Europe. In October, this positive bias band has shifted towards the Southern Hemisphere, forming a positive latitudinal bias belt between 10 and 30° S over land and sea. Strong negative biases are observed over the Canadian boreal forests. The latter biases disappear in April, while the positive biases over the ocean decrease in magnitude. Strong positive biases are now observed over eastern Europe. In July, the previous 20° N oceanic positive bias belt relocates to the Southern Hemisphere, while over land strong positive biases are observed in northern Egypt, east of the Caspian Sea, and the central and eastern United States. Strong negative biases occur over Indonesia and the northern Pacific, although we note that the most significant biases occur at $> 60°$ N, which is outside of the LMD domain.

Figure 7 shows (same as the bottom row in Fig. 6) the differences in the respective biases of LMD and RAL_LMDavk with respect to CAMS for different months (January, April, July, and October) but now also for several years (2008, 2010, 2012, and 2014). One immediate observation is that the average LMD–RAL difference in their respective biases towards CAMS becomes ever more positive when moving from 2008 to 2014. This is consistently seen for all months. We did not apply any correction to the 2014 RAL data, so

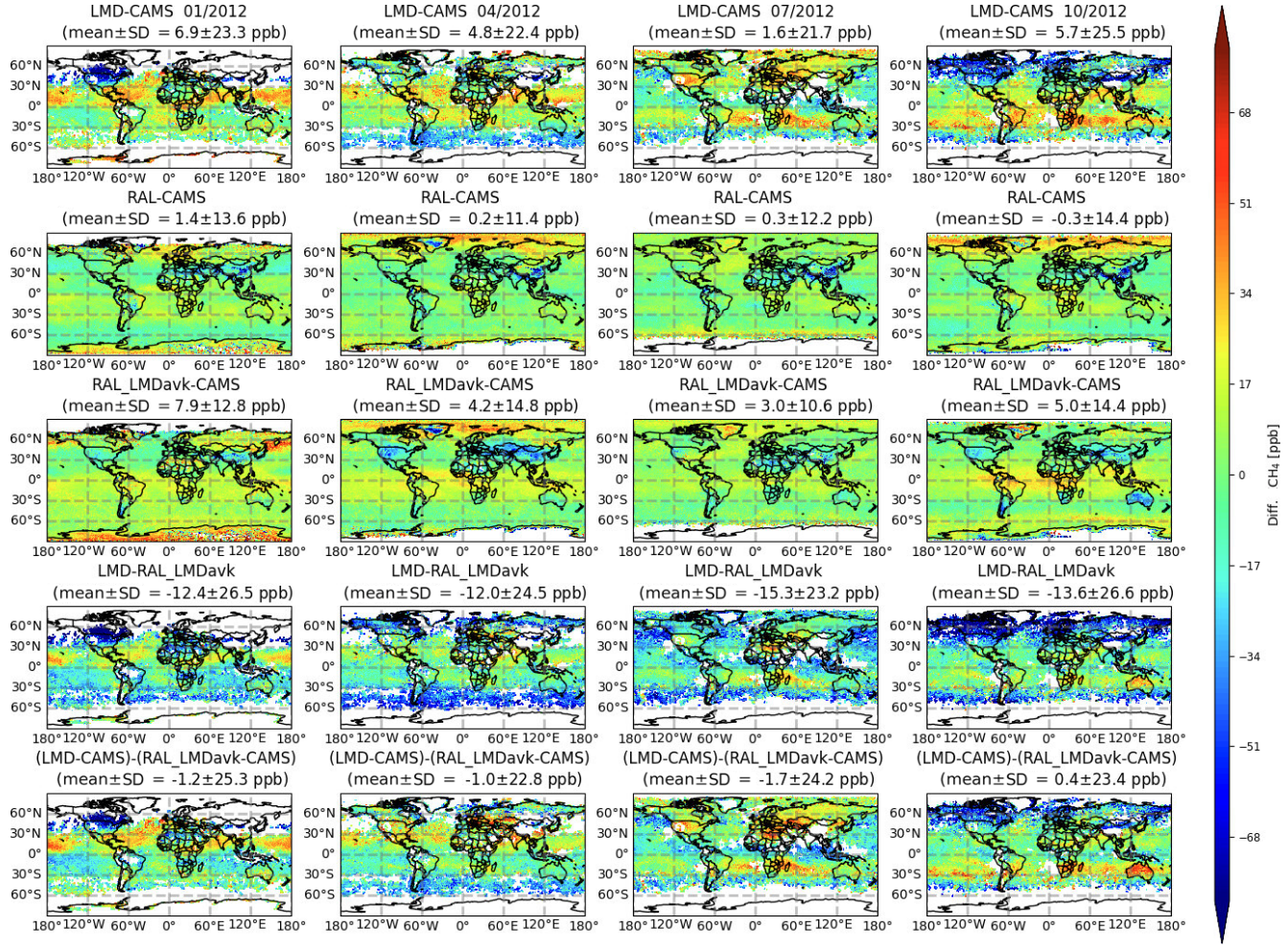


**Figure 6.** Global monthly mean maps for January, April, July, and October 2012 (columns from left to right). The top row shows the LMD–CAMS daytime mt$CH_4$ difference; the second and third row show the same but for RAL and RAL_LMDavk X(mt)$CH_4$, respectively. The last three rows show the intercomparison between the satellite products. Row 4 shows the LMD–RAL difference and row 5 LMD–RAL_LMDavk, while the last two rows compare the respective differences in LMD and RAL_LMDavk to their respective CAMS fields.

its discontinuity could be at play, but the trend is also clearly visible when moving from 2008 to 2012. This points to a temporal stability issue with either LMD, RAL, or both. The magnitude of these overall averaged bias shifts amounts to a 2.3 ppb $yr^{-1}$ (January), 2.1 ppb $yr^{-1}$ (April), 1.1 ppb $yr^{-1}$ (July), and 1 ppb $yr^{-1}$ (October) shift. The marked differences between January–April, on the one hand, and July–October, on the other hand, also allude to a seasonal error component.

While we do see shifts in the magnitude of some features (for instance, in January and October we clearly see ever stronger positive biases over Australia), no major shifts in the overall patterns are observed. For instance, all years still feature strong negative biases over the Canadian boreal forests in January and October, and all years show the positive bias band (in January, positioned between 10 and 30° N, and in October, between 10 and 30° S). A new feature that can be clearly observed in the 2014 (last row) data is the emergence of a, somewhat weaker but still clearly positive, second bias band in the opposite hemispheres (in January, positioned between 10 and 30° S, and in October, between 10 and 30° N). The emergence of this second band is also already apparent in 2012.

### 5.2 Long-term trend and seasonal variation

The observation of clear changes in the biases as a function of time in Fig. 7 prompts the exploration of the long-term trends and seasonal variations in both LMD and RAL. The $CH_4$ annual growths derived from LMD and uncorrected RAL (thus ignoring the discontinuity for now) are compared to each other (Fig. 8). Due to the cloud contamination and post-filtering, the $CH_4$ measurements are not always available, even though we use the monthly averaged data. In this section, we only consider the trend on the $1° \times 1°$ grid

where there are fewer than 12 absent monthly means during these 8 years. The $mtCH_4$ trends derived from the LMD data are generally available in the low-latitude regions, while the $XCH_4$ trends derived from the RAL are calculated in most places, except for the polar region. The mean and SD of the $CH_4$ annual growth rates are $6.43 \pm 1.34$ ppb yr$^{-1}$ and $4.06 \pm 0.66$ ppb yr$^{-1}$, as derived from the LMD and RAL data, respectively. The mean difference in the $CH_4$ trend from LMD and RAL measurements is 2.54 ppb yr$^{-1}$, which is larger than the SD of their differences of 1.53 ppb yr$^{-1}$. After smoothing the RAL data with the LMD weighting function (RAL_LMDavk), the $mtCH_4$ trend derived from the RAL_LMDavk is $4.29 \pm 0.86$ ppb yr$^{-1}$, which is larger than the $XCH_4$ trend derived from the original RAL data. The mean difference in the $mtCH_4$ trend between LMD and RAL_LMDavk reduces to 1.63 ppb yr$^{-1}$ but is still larger than the SD of their differences (1.33 ppb yr$^{-1}$).

The global maps of $CH_4$ annual growth rates are also derived from LMD and RAL nighttime measurements (not shown here). The spatial distributions of the $CH_4$ trend derived from the daytime and nighttime measurements are similar for both LMD and RAL. Moreover, the global mean and SD of the $CH_4$ trend derived from nighttime measurements are 6.65 and 1.46 ppb yr$^{-1}$, as derived from the LMD data, and are 4.01 and 0.68 ppb yr$^{-1}$, as derived from the RAL data, which are close to the results derived from daytime measurements. As the results from daytime and nighttime measurements are consistent, we only discuss the trends of $CH_4$ derived from the RAL and LMD daytime measurements in the following sections.

The time series and seasonal variation in $CH_4$ are further investigated based on TransCom (Fig. 9) (Gurney et al., 2002), which has been used in the Carbon Tracker $CH_4$ model (Bruhwiler et al., 2014), including 11 land (Fig. 10) and 11 ocean (Fig. 11) regions. A 6.7 ppb post-16-May-2023 correction has been applied to the RAL total column data. Here, however, we mainly focus on LMD and RAL_LMDavk $mtCH_4$ measurements. At land regions, it is found that the seasonal variations in $mtCH_4$ from LMD and RAL_LMDavk measurements are generally close to each other in the low-latitude regions but are different in the high-latitude regions. Specifically, the seasonal variations in $mtCH_4$ from LMD and RAL_LMDavk measurements are close to each other in South American tropical, South American temperate, northern Africa, Eurasia temperate, and tropical Asia regions, while they are different in the North American boreal and temperate regions, Europe, Southern Africa, Eurasia boreal region, and Australia. The $mtCH_4$ annual growths derived from LMD are 0.4–1.8 ppb yr$^{-1}$ larger than RAL_LMDavk in most regions, except for the North American boreal and Eurasia boreal regions. The $mtCH_4$ annual growth derived from LMD has a strong latitude dependence, which is close to 6 ppb yr$^{-1}$ in the tropical region but smaller than 3 ppb yr$^{-1}$ in the high-latitude regions. At ocean regions, it is found that the seasonal variations in $mtCH_4$ from LMD and RAL_LMDavk measurements are close to each other in most regions, except for the Northern Ocean and North Atlantic temperate region. At the Southern Ocean and South Pacific temperate region, the phases of the seasonal variations in $mtCH_4$ from the LMD and RAL_LMDavk measurements are similar, but the amplitudes of the seasonal variation in $mtCH_4$ derived from the LMD measurements are larger than those derived from the RAL_LMDavk data. The $mtCH_4$ annual growths derived from LMD are 0.3–2.2 ppb yr$^{-1}$ larger than RAL_LMDavk in most ocean regions, except at the Southern Ocean.

The above analysis shows that the annual growth of $mtCH_4$ derived from the uncorrected RAL data between July 2007 and June 2015, while generally consistent between regions, is systematically smaller than that of LMD. While we could not clearly extract a correction factor for the 16 May 2013 RAL discontinuity with regards to the LMD-smoothed RAL_LMDavk $mtCH_4$ values (see Sect. 3.7), the here-observed discrepancies nevertheless prompt us to produce trend estimates based on two individual linear trends for the two periods before and after 16 May 2013. We then average, using the covered time frames as weights, the two estimates to get an overall corrected value for the trend.

Table 3 lists all the trends of $CH_4$ between July 2007 and June 2015 derived from LMD, RAL_LMDavk, and RAL_LMDavk (two periods) at nine TransCom low- and mid-latitude land regions. The weighted mean of the annual growths of $XCH_4$ becomes 5.6 ppb yr$^{-1}$ when using the RAL data before and after 16 May 2013. This result is close to the $mtCH_4$ annual growth of 5.3 ppb yr$^{-1}$ between July 2007 and June 2015 observed by the LMD data. The mean $XCH_4$ annual growth derived from the RAL data between July 2013 and June 2015 is 9.5 ppb yr$^{-1}$, which is larger than that of 4.4 ppb yr$^{-1}$ between July 2007 and May 2013. The $CH_4$ annual growth rate derived from the NOAA surface in situ measurements between June 2013 and June 2015 is 11.2 ppb yr$^{-1}$, which is also larger than that of 5.6 ppb yr$^{-1}$ between July 2007 and May 2013.

To further explore the observed RAL and LMD differences, as well as the impact (if any) of the discontinuity corrections, Fig. 12 shows the long-term trend (Fig. 12a–c) and seasonal cycle amplitudes (Fig. 12d) of the respective LMD, RAL, and RAL_LMDavk satellite product and CAMS biases grouped per 10° latitude band. Figure 12a shows the behaviour of all data as is, Fig. 12b when applying a +6.7 ppb correction onto the post-16-May-2013 RAL total column data, and Fig. 12c when splitting the RAL total column and RAL_LMDavk into two independent time series. Uncorrected (Fig. 12a), the overall trend of the RAL_LMDavk–CAMS bias shows no significant latitudinal dependence, while RAL features higher values at high latitudes. When applying a 6.7 ppb correction (Fig. 12b), the RAL values shift upwards (less negative values) by approximately 1 ppb. When splitting the RAL–CAMS and RAL_LMDavk–CAMS data into two independent time series (Fig. 12c), we see

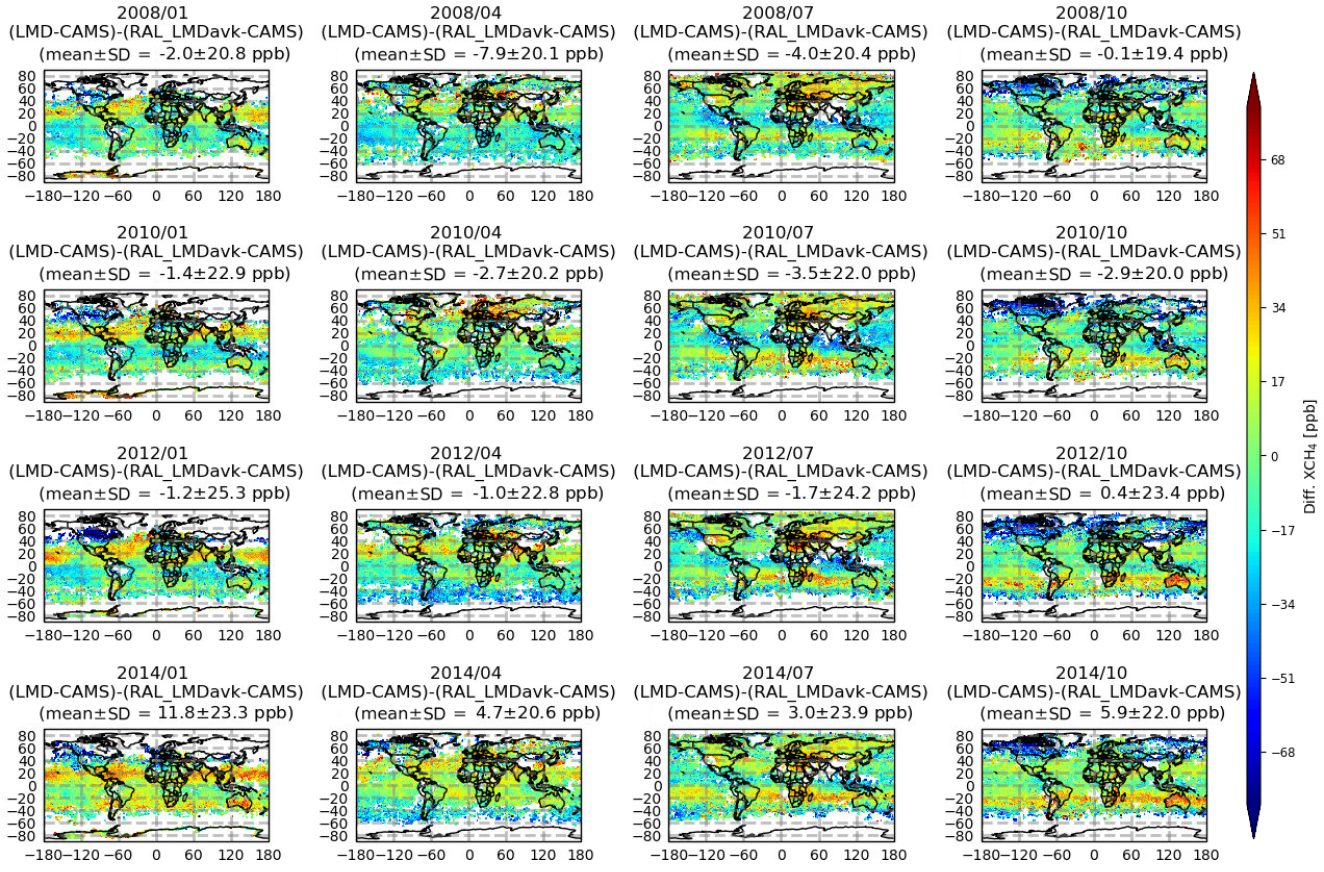


**Figure 7.** Global monthly mean maps for January, April, July, and October (columns from left to right) of the respective differences in LMD and RAL_LMDavk to their respective CAMS fields for 2008, 2010, 2012, and 2014 (rows).

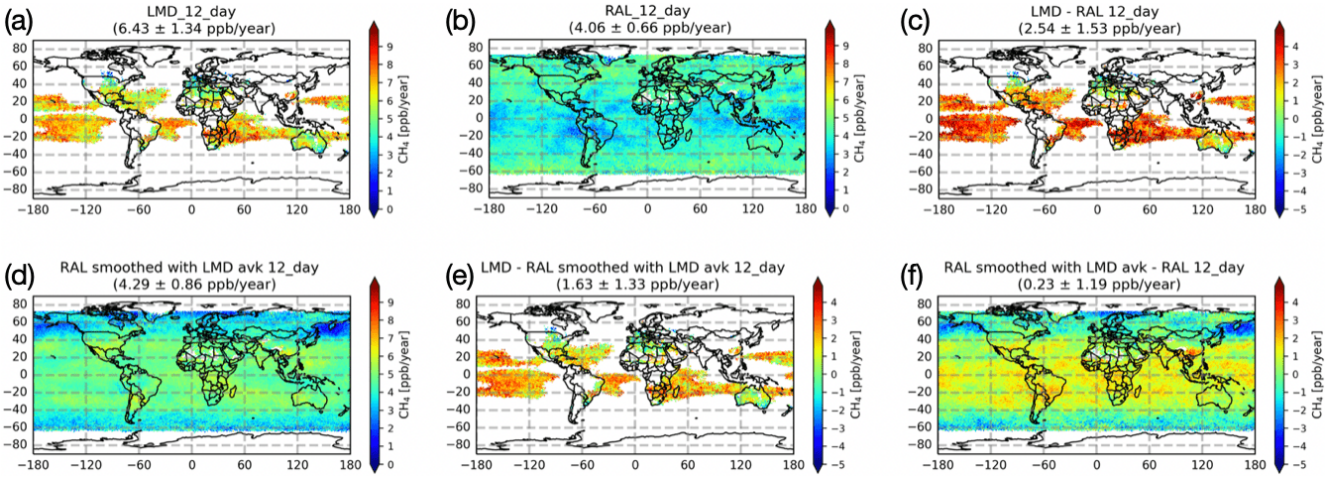


**Figure 8.** The mt(X)$CH_4$ annual growth derived from LMD **(a)**, RAL **(b)**, and RAL_LMDavk **(d)** daytime measurements, together with their difference between LMD and RAL **(c)**, between LMD and RAL_LMDavk **(e)**, and between RAL and RAL_LMDavk **(f)**. The $CH_4$ annual growth is only calculated for grid boxes with fewer than 12 months of missing data between July 2007 and June 2015. No RAL discontinuity correction was applied.

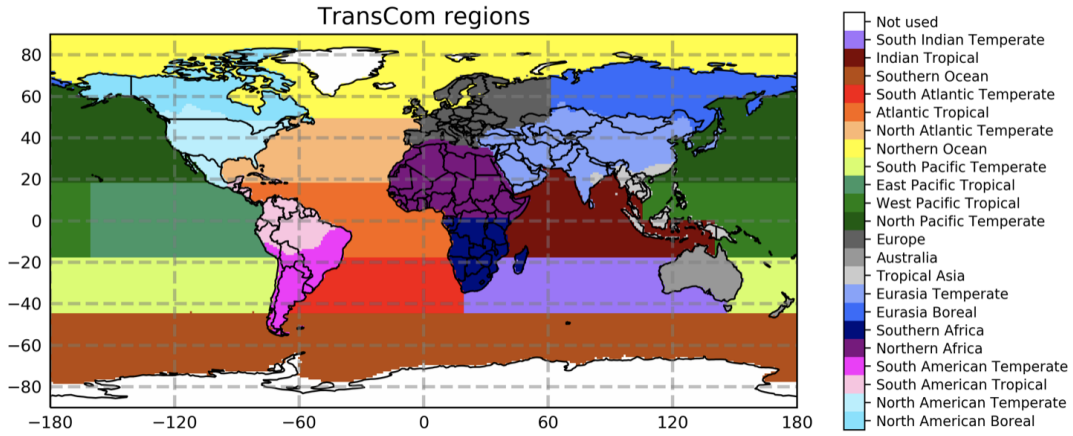


**Figure 9.** The TransCom map including 11 land regions and 11 ocean regions.

**Table 3.** The trend of $CH_4$ (in units of ppb $yr^{-1}$) between July 2007 and June 2015 derived from LMD, RAL_LMDavk, and RAL_LMDavk (two periods) at nine TransCom low- and mid-latitude land regions.

| Region | LMD | RAL_LMDavk | RAL_LMDavk (two periods) | |
|---|---|---|---|---|
| | | | 2007.7–2013.5 | 2013.6–2015.6 |
| North American temperate | $4.8 \pm 0.8$ | $4.2 \pm 0.7$ | $4.1 \pm 1.5$ | $9.3 \pm 4.1$ |
| South American tropical | $5.0 \pm 1.1$ | $3.8 \pm 0.7$ | $4.2 \pm 1.2$ | $10.0 \pm 6.6$ |
| South American temperate | $5.2 \pm 0.7$ | $4.4 \pm 0.5$ | $4.0 \pm 0.5$ | $12.4 \pm 5.5$ |
| Europe | $4.0 \pm 1.0$ | $3.6 \pm 0.7$ | $3.8 \pm 1.4$ | $6.2 \pm 2.1$ |
| Northern Africa | $5.5 \pm 1.2$ | $4.5 \pm 0.7$ | $4.5 \pm 1.5$ | $9.1 \pm 1.8$ |
| Southern Africa | $6.3 \pm 0.8$ | $4.5 \pm 0.9$ | $4.5 \pm 1.1$ | $11.8 \pm 7.8$ |
| Eurasia temperate | $4.9 \pm 1.4$ | $4.1 \pm 0.9$ | $4.3 \pm 1.6$ | $7.5 \pm 4.8$ |
| Tropical Asia | $5.7 \pm 1.3$ | $4.4 \pm 0.8$ | $5.3 \pm 1.3$ | $9.6 \pm 5.5$ |
| Australia | $6.0 \pm 0.6$ | $4.5 \pm 0.5$ | $4.5 \pm 0.9$ | $9.4 \pm 1.9$ |
| Mean | 5.3 | 4.2 | 4.4 | 9.5 |
| | | | 5.6 | |

the strongest impact, with the RAL bias shifting further upwards by another $\sim 1$ ppb. For RAL_LMDavk, not only a bias shift is observed, but also the shape has changed considerably (from a constant offset to one which shows much weaker negative biases near the poles). It appears that the impact of the latter correction is much stronger near the poles ($\sim 3$ ppb) than at the (sub)tropics ($\sim 1$ ppb). Implementing a stronger (instead of 6.7 ppb, a 10 ppb shift) correction into both RAL time series does bring the outcome of the two correction methods closer to one another; however, the change in the shape of RAL_LMDavk (using two independent time series) with respect to its latitudinal dependence on the long-term trend could not be replicated with a simple bias correction. Moreover, such a significant change would certainly have been picked up in our analysis (see Sect. 3.7).

Using the last correction method (two independent time series), all three algorithms show similar trend values near the (sub)tropics between 30° N and 30° S. Further north and south, however, LMD–CAMS shows markedly ever stronger negative trend values when moving towards the poles. We see little to no impact of the correction methods on the observed seasonal cycle amplitudes of the respective satellite–CAMS bias (Fig. 12d). It shows that the amplitude of the seasonal cycle in the RAL–CAMS and RAL_LMDavk–CAMS residuals is consistently lower than for LMD–CAMS. This points to a significant difference between the seasonal cycle phases or amplitudes of both products. Also of interest is the observation of a strong increase in the LMD–CAMS residual seasonal amplitudes at higher ($> 50°$) latitudes in line with LMD's very strong decrease in the residual trend at latitudes exceeding (40°) in both hemispheres (Fig. 12d).

### 5.3 Short summary

Our analysis of the direct comparisons between RAL and LMD paint a rather complex picture with observed and marked differences both in space and time. Important to note is that even when smoothing RAL with the LMD sensi-

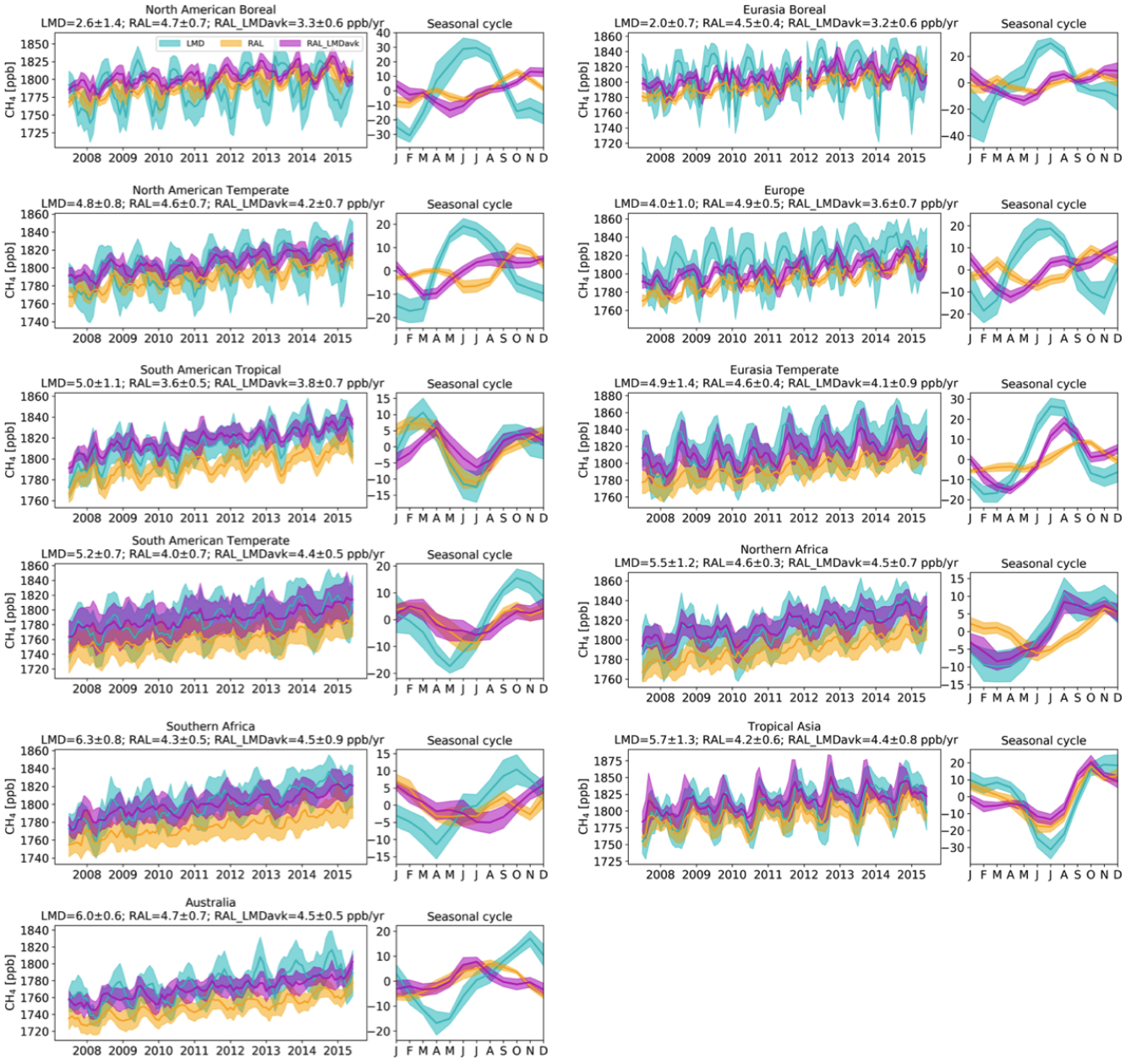


**Figure 10.** The time series of the LMD, RAL (+6.7 ppb discontinuity correction applied), and RAL_LMDavk $CH_4$ monthly means (solid lines) and standard deviations (shadow), together with the seasonal variations in $CH_4$ at 11 land TransCom regions.

tivity profile, vertical sensitivity differences with LMD remain as shown by the difference when comparing LMD and RAL_LMDavk directly or their respective biases towards CAMS. Adding further complexity is the impact of RAL's 16 May 2013 discontinuity, which, depending on the correction method used, impacts the long-term trend by 1 to 2 ppb $yr^{-1}$. Some of the most marked RAL–LMD differences observed point to a significant shift in the amplitude and/or phase of their respective seasonal cycles, particularly at higher latitudes. The North American temperate region, Europe, and the Northern Ocean in Figs. 10 and 11 are prime examples. Also, at higher latitudes, we see ever stronger differences in the long-term trends of both products.

## 6 Comparisons with independent reference data

In this section, we compare RAL (discontinuity-corrected) and LMD data with in situ data from HIPPO, IAGOS, and AirCore, as well as ground-based remote-sensing data from the TCCON and NDACC networks. Note that given the complex nature of the RAL–LMD differences (both in time

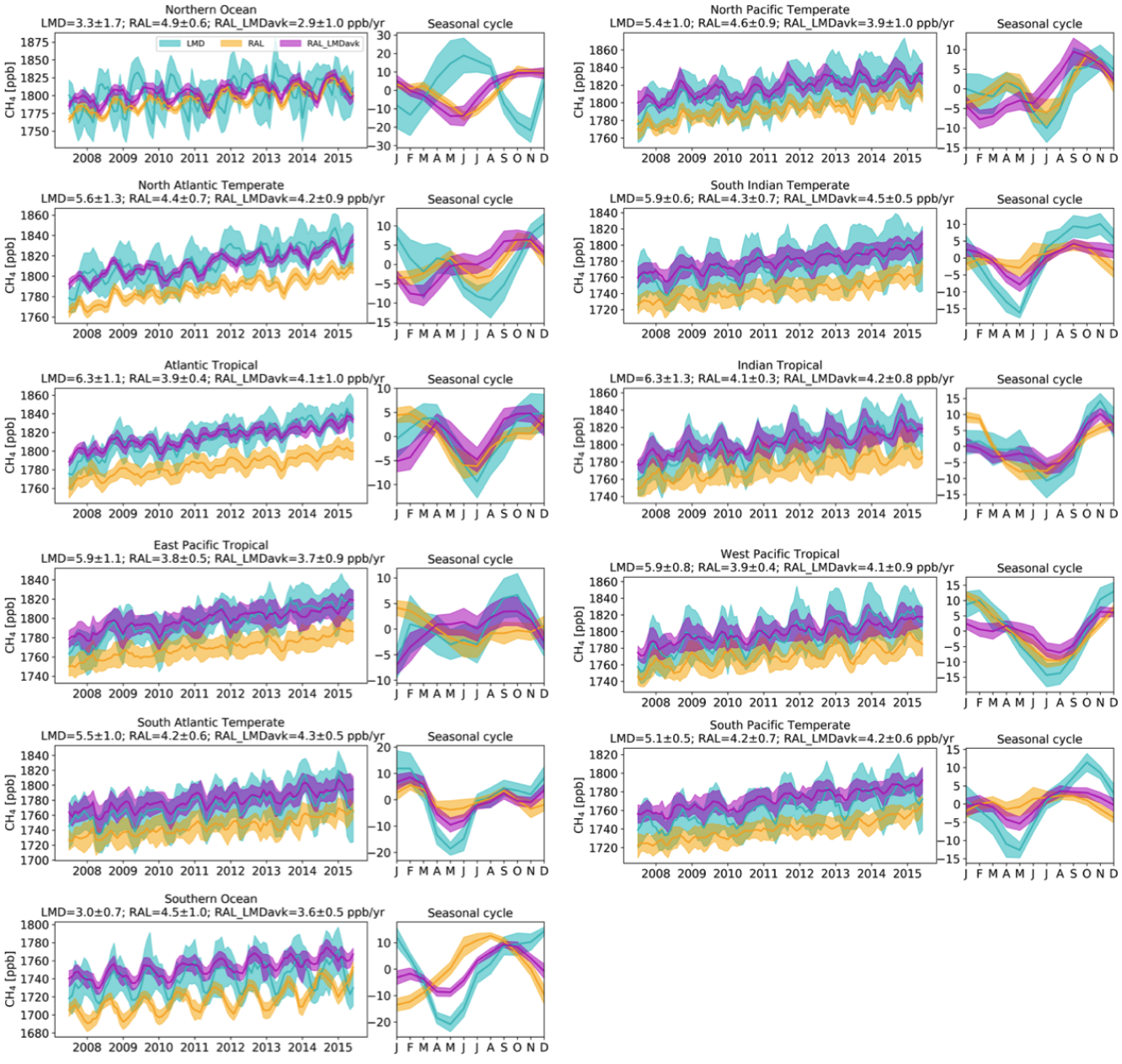


**Figure 11.** Same as Fig. 10 but at 11 ocean TransCom regions.

and in space), any obtained difference observed between the satellite and reference measurements depends on the time and location of the reference measurements in question. For instance, HIPPO measurements focused largely on the Pacific Ocean and are often measured near the poles. IAGOS profiles are taken during ascent and descent from/towards airports and are thus tilted towards more urban environments. AirCore is restricted to just a few locations in the United States, Aotearoa / New Zealand, and Finland (see Fig. 1). There are also large differences with respect to the time periods covered.

### 6.1 Comparisons with in situ profiles

In this section, LMD mt$CH_4$ and RAL X$CH_4$ are compared to the in situ profiles. We also look at RAL's 0–6 km and 6–12 km q$CH_4$ partial columns. The latter is possible as the degrees of freedom (DOFs) of the RAL $CH_4$ profile is about 2.0, with two distinct pieces of information in the partial columns of 0–6 km and 6–12 km.

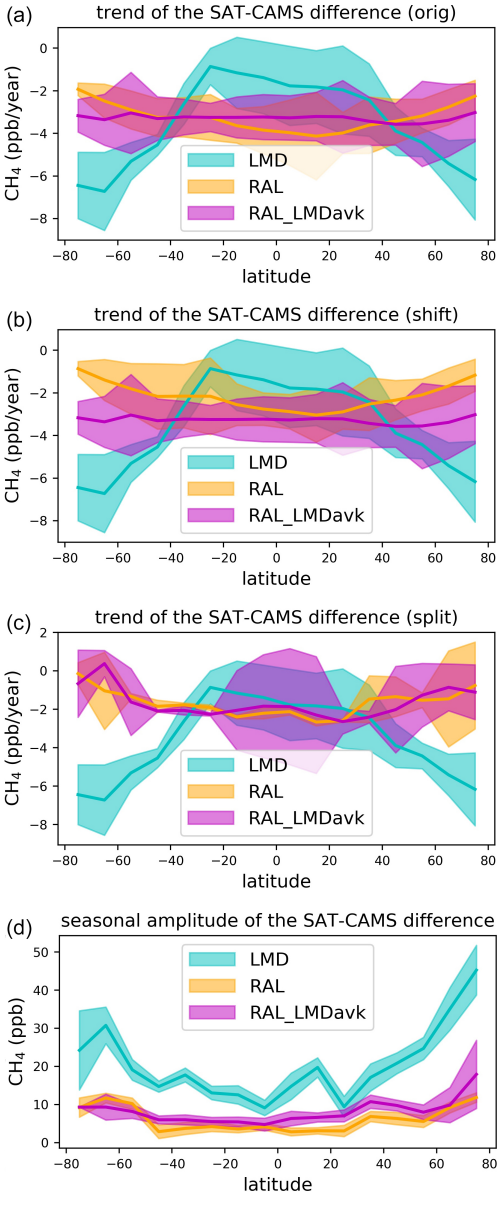


**Figure 12.** **(a)** Long-term trend values (ppb $yr^{-1}$) for the satellite–CAMS residuals for 10° wide latitude bands for discontinuity uncorrected measurements. **(b)** Same as panel **(a)** but now with a +6.7 ppb RAL discontinuity correction. **(c)** Same as panel **(a)** but now with RAL and RAL_LMDavk split into a pre- and post-16-May-2013 time series. The overall trend values corresponds with the time-weighted average of the trends from these two time series. **(d)** Seasonal cycle amplitude of the satellite–CAMS residuals for 10° wide latitude bands.

### 6.1.1 RAL total column

The RAL and HIPPO $XCH_4$, together with their differences along with the latitude, are shown in Fig. 13. Both RAL and HIPPO measurements observe high $XCH_4$ in the Northern Hemisphere and low $XCH_4$ in the Southern Hemisphere. Specifically, the $XCH_4$ at 40° N is about 80 ppb larger than that at 40° S. Two $XCH_4$ peaks at about 35 and 75° N are captured by both datasets. Only 49 out of 466 (10.5 %) differences between RAL and HIPPO measurements are outside their combined 1 $\sigma$ uncertainties. However, the mean of the HIPPO measurements is 16.5 ppb larger than the mean of RAL measurements between 15° N and 15° S, with many differences beyond the combined uncertainties. The overall mean and SD of the differences between RAL and HIPPO measurements are −4.6 and 16.5 ppb, respectively. The scatter plot between RAL and HIPPO measurements shows that the correlation coefficient ($R$) is 0.84, indicating there is a good agreement between RAL and HIPPO measurements. The linear fit suggests that the RAL data are slightly smaller/greater than the HIPPO measurements when the $XCH_4$ is low/high. Note that since all HIPPO measurements occurred prior to 16 May 2013, no correction method needed to be applied.

Furthermore, the RAL $XCH_4$ are also compared to IAGOS and AirCore (not shown here). Here we did apply a +6.7 ppb correction on the post-16-May-2013 data. The mean and SD of the differences between RAL and IAGOS measurements are −1.6 and 21.9 ppb, respectively (note that without correction, the bias equaled $-4.8 \pm 23.0$ ppb). The $R$ between the RAL and IAGOS measurements is 0.52. Of the 260 differences between RAL and IAGOS measurements, 222 are within their combined 1 $\sigma$ uncertainties. The mean and SD of the differences between RAL and AirCore measurements are −4.4 and 14.1 ppb, respectively (uncorrected the bias equals $-10.2 \pm 14.5$ ppb). The $R$ between RAL and AirCore measurements is 0.83, and the linear fit is close to the one-by-one line, indicating that there is a good agreement between the RAL and AirCore measurements. Indeed, 45 out of 49 differences between RAL and AirCore measurements are within their combined uncertainties. Of the three in situ reference datasets, IAGOS typically features the lowest correlation coefficient ($R$) and highest SD of the differences. This is due to a combination of having a far greater distribution around the globe and having profiles that are taken at or near urban centres (and thus local emission sources) instead of remote locations. Its profiles also typically require more extrapolation.

### 6.1.2 LMD mid-tropospheric column

Figure 14 shows the LMD and HIPPO $mtCH_4$, together with their differences and the latitude. The data density of the LMD data is much less than the RAL data, but co-located LMD measurements are still able to observe the high $mtCH_4$ in the Northern Hemisphere and the low $mtCH_4$ in the Southern Hemisphere, as expected. LMD nicely captures the overall latitudinal distribution of $CH_4$ with no obvious issues. As already mentioned in Sect. 3.4, the SD of the co-located LMD measurements is calculated as the retrieval uncertainty in the LMD data because of no reported uncertainty. As a result, 34 out of 97 differences between LMD and HIPPO

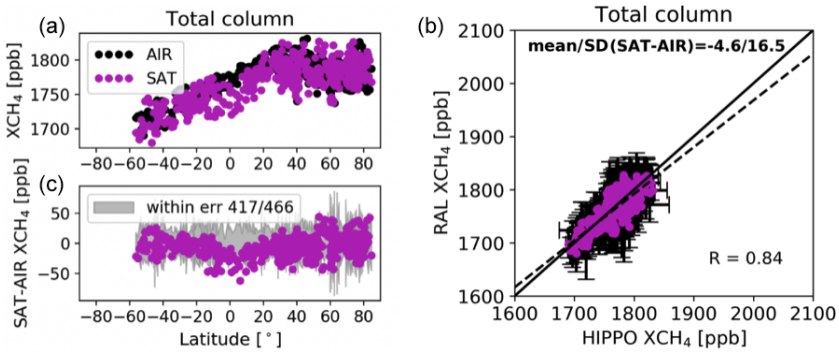


**Figure 13.** RAL (no data after May 2013) and HIPPO $XCH_4$, together with their differences at different latitudes **(a, c)**, and the scatter plot between the RAL and HIPPO $XCH_4$ **(b)**. $R$ is the correlation coefficient. The dotted and solid lines correspond with a linear fit through the data and a $y = x$ line, respectively.

measurements are within their combined uncertainties. The mean and SD of the differences between LMD and HIPPO measurements are −10.9 and 27.7 ppb, respectively. The $R$ between LMD and HIPPO measurements is 0.48.

Similarly, the IAGOS and AirCore measurements are used to compare with co-located LMD data. The mean and SD of the differences between LMD and IAGOS measurements are 2.3 and 30.6 ppb, respectively. The $R$ between LMD and IAGOS measurements is 0.49. Only 27 out of 58 differences between LMD and IAGOS measurements are within their combined uncertainties. Only three co-located LMD and AirCore values are selected, and two out of three differences between LMD and AirCore measurements are within their combined uncertainties. The mean and SD of the differences between LMD and AirCore measurements are −0.3 and 15.2 ppb, respectively. The $R$ between LMD and AirCore measurements is 0.60.

The mean and SD of the differences, together with the $R$ and $N$ (the number of measurement pairs), are summarized in Table 4.

### 6.1.3 RAL partial columns

Figure 15 shows the RAL and HIPPO $qCH_4$, together with their differences and the latitude in the vertical ranges of 0–6 km and 6–12 km. Again, we have to note that the HIPPO vertical profiles have been expanded with scaled CAMS model data. The mean and SD of the differences between RAL and HIPPO measurements in the 0–6 km layer are −12.2 and 26.5 ppb, respectively. The mean and SD of the differences between RAL and HIPPO measurements in the 6–12 km layer are −1.6 and 22.2 ppb, respectively. The $R$ between RAL and HIPPO measurements is 0.87 and 0.76 in the 0–6 km and 6–12 km layers. The 0–6 km partial column (Fig. 15a–c) shows a consistent $qCH_4$ upward trend with latitude in the Northern Hemisphere. For the 6–12 km partial column (Fig. 15d–f), two $qCH_4$ concentration peaks can be observed around 35 and 75° N. The HIPPO measurements are larger than the RAL data in the 0–6 km layer. For this layer, 325 out of 466 differences between RAL and HIPPO measurements are within their combined uncertainties, and the underestimation of RAL measurements is particularly found in the tropical region. For the 6–12 km layer, 343 out of 466 differences between RAL and HIPPO measurements are within their combined uncertainties, and the RAL and HIPPO measurements are close to each other in the tropical region. The SD of the differences between the RAL and HIPPO measurements in both partial columns are larger than in the total column, reflecting that the uncertainties in the partial columns (0–6 km and 6–12 km) are larger than that of the total column.

The mean and SD of the differences between RAL measurements and IAGOS (expanded with scaled CAMS model data) in the 0–6 km layer are −5.0 and 35.1 ppb, respectively. The mean and SD of the differences between RAL and measurements in the 6–12 km layer are −3.2 and 22.7 ppb, respectively (without the discontinuity correction; here +9.6 ppb for the 0–6 km layer and +3.6 ppb for the 6–12 km layer, respectively; the biases were $-9.5 \pm 36.0$ ppb and $-4.9 \pm 23.2$ ppb for the 0–6 km and 6–12 km layer, respectively). The $R$ between RAL and IAGOS measurements is 0.60 and 0.54 in the 0–6 km and 6–12 km layers. For the lower layer (0–6 km), 179 out of 260 differences between RAL and IAGOS measurements are within their combined uncertainties. For the upper layer (6–12 km), 158 out of 260 differences between RAL and IAGOS measurements are within their combined uncertainties. The mean and SD of the differences between RAL and AirCore measurements in 0–6 km are −14.3 and 26.3 ppb (uncorrected −22.5 and 27.1 ppb), respectively. The mean and SD of the differences between RAL and AirCore measurements in the 6–12 km layer are −7.5 and 26.1 ppb (uncorrected −10.6 and 26.1 ppb), respectively. The $R$ is 0.77 and 0.52 in the 0–6 km and 6–12 km layers. For the lower layer (0–6 km), 37 out of 49 differences between RAL and AirCore measurements are within their combined uncertainties in 0–6 km. Only 22 out

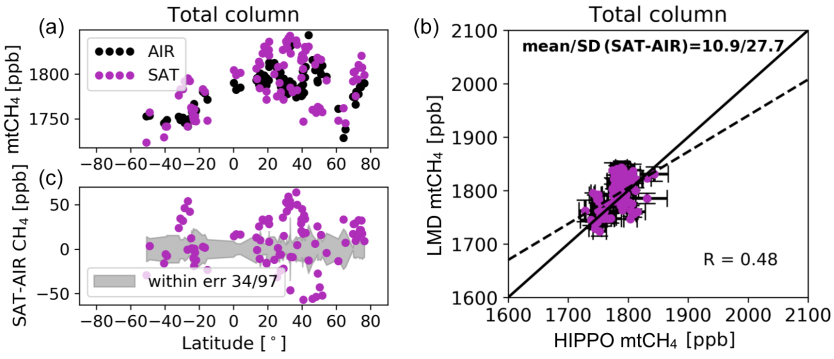


**Figure 14.** Same as Fig. 13 but for LMD and HIPPO measurements.

**Table 4.** The mean and SD of the difference between in situ profile measurements (AIR) and IASI satellite $CH_4$ measurements (SAT). RAL measurements feature a discontinuity correction.

| In situ | IAGOS | | AirCore | | HIPPO | |
|---|---|---|---|---|---|---|
| Satellite | LMD | RAL | LMD | RAL | LMD | RAL |
| Mean (SAT–AIR) [ppb] | 2.3 | −1.6 | −0.3 | −4.4 | 10.9 | −4.6 |
| SD (SAT–AIR) [ppb] | 30.6 | 21.9 | 15.2 | 14.1 | 27.7 | 16.5 |
| $R$ | 0.49 | 0.52 | 0.60 | 0.83 | 0.48 | 0.84 |
| $N$ | 58 | 260 | 3 | 49 | 97 | 466 |

of 49 differences between RAL and AirCore measurements are within their combined uncertainties in 6–12 km. The standard deviation and $R$ results for IAGOS are again markedly worse than for HIPPO and AirCore.

A summary of the RAL partial column comparison results with in situ profile measurements are listed in Table 5.

One striking feature, observable in the 0–6 km bias as a function of the latitude plot (Fig. 15a and c), is a marked negative bias with respect to HIPPO near the Equator. This corresponds with our observations using the CAMS model (Fig. 5d–f), where a narrow band of negative RAL–CAMS biases can be seen over the Pacific Ocean near the Equator in nearly all seasons.

## 6.2 Comparisons with ground-based FTIR measurements

Here we compared the LMD and RAL methane data products with ground-based remote-sensing data from the TCCON and NDACC networks. As with the in situ comparisons, a +6.7 ppb correction has been applied to the RAL post-16-May-2013 data. Also note that there is substantial difference in the time periods covered by the individual stations. For TCCON, the stations that cover almost the entire time period (< 2.5 years of missing data), and henceforth referred to as core stations, are Sodankylä, Białystok, Orléans, Garmisch, Park Falls, Lamont, Izaña, Darwin, Wollongong, and Lauder. Other stations, on the other hand, have noticeably shorter coverages (Rikubetsu and Edwards, for instance, have < 2 years of co-located measurements). For NDACC, all stations are listed as core stations as they seem to cover the entire time period, apart from Maïdo (2.5 years of data), which is excluded. Note that both Mauna Loa and Saint-Denis feature some large (> 1 year) data gaps in their time series and that, even with a long time span, the number of co-located data pairs may differ greatly between stations. For instance, at high-latitude sites (Eureka and Thule), annual gaps occur in the dataset during wintertime (see Figs. 16 and 17). For RAL, the amount of pre- versus post-discontinuity data largely determines the magnitude of the impact of the applied discontinuity correction, and therefore, when comparing average overall long-term trends, we have restricted ourselves to the so-called core stations which cover a substantially long time period (as listed above).

### 6.2.1 RAL bias and scatter

As the ground-based FTIR measurements (both TCCON and NDACC) have limited vertical information in the troposphere, we only focus on the total column of RAL in this section. Figure 16a shows the time series (16 May 2013 uncorrected) of the differences between the RAL IASI and TCCON 2-week means at 21 sites between July 2007 and June 2015. The sites are sorted by their latitudes from north to south. The absolute mean and SD of the +6.7 ppb corrected differences (RAL–TCCON) at all sites are 5.05 and 11.23 ppb (uncorrected equated to 4.31 and 11.28 ppb), respectively. The differences are within ±20 ppb, and there is

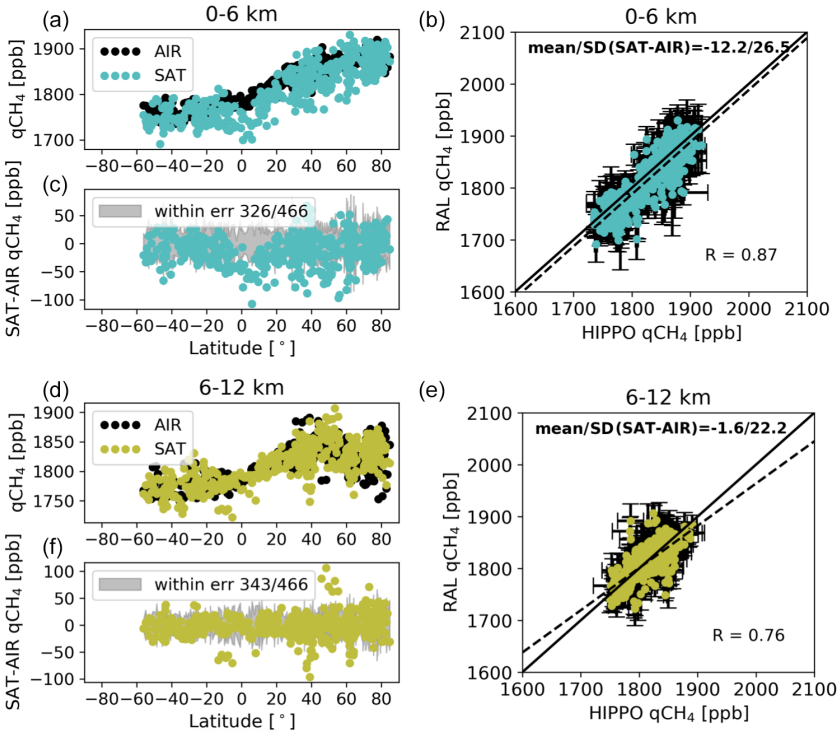


**Figure 15.** RAL and HIPPO $qCH_4$, together with their differences at different latitudes **(a, c, d, f)**, and the scatter plot between the satellite and HIPPO $qCH_4$ in the vertical ranges between 0 and 6 km (**a–c**; no data after May 2013), and between 6 and 12 km (**d–f**; no data after May 2013). **(b, e)** $R$ is the correlation coefficient. The dotted and solid lines correspond with a linear fit through the data and a $y = x$ line, respectively.

**Table 5.** The mean and SD of the difference between IASI RAL partial columns (a bias correction has been implemented) and in situ values.

| In situ | IAGOS | | AirCore | | HIPPO | |
|---|---|---|---|---|---|---|
| RAL | 0–6 km | 6–12 km | 0–6 km | 6–12 km | 0–6 km | 6–12 km |
| Mean (SAT–AIR) [ppb] | −5.0 | −3.2 | −14.3 | −7.5 | −12.2 | −1.6 |
| SD (SAT–AIR) [ppb] | 35.1 | 22.7 | 26.3 | 26.1 | 26.5 | 22.2 |
| $R$ | 0.60 | 0.54 | 0.77 | 0.52 | 0.87 | 0.76 |
| $N$ | 260 | 260 | 49 | 49 | 466 | 466 |

no clear seasonal variation in the differences at most sites. For high-latitude sites (Eureka and Sodankylä), the RAL $XCH_4$ is larger than the TCCON measurements, especially in spring. Ostler et al. (2014) pointed out that the smoothing error in the TCCON $XCH_4$ retrieval is large under the polar vortex situation, and the TCCON measurement is about 40 ppb larger than the real status. However, we find that the RAL $XCH_4$ is even larger than the TCCON measurement in spring at high-latitude sites. The time series of the differences between the RAL IASI and NDACC measurements at 13 sites are also shown in Fig. 16b. The mean and SD of the (discontinuity-corrected) differences are 9.79 and 15.26 ppb (uncorrected 9.55 and 15.82 ppb), respectively. Similar to the TCCON comparison, for the low- and mid-latitude sites, it is found that there is little latitude dependence in the difference between RAL and NDACC measurements, and the differences are within ±20 ppb. However, in high-latitude sites (> 60° N), the RAL $XCH_4$ is 20–100 ppb and systematically larger than the NDACC measurements at Thule, and the RAL $XCH_4$ is generally larger than the NDACC measurements in spring at Kiruna.

### 6.2.2 LMD bias and scatter

Figure 17 shows the time series of the differences between LMD IASI and the ground-based FTIR measurements between July 2007 and June 2015. Compared to RAL measurements, there are no available co-located LMD measurements at the Eureka, Rikubetsu, and Edwards TCCON sites. The mean and SD of the differences are −4.76 and 16.32 ppb, respectively. It is noted that the mean differences vary with lat-

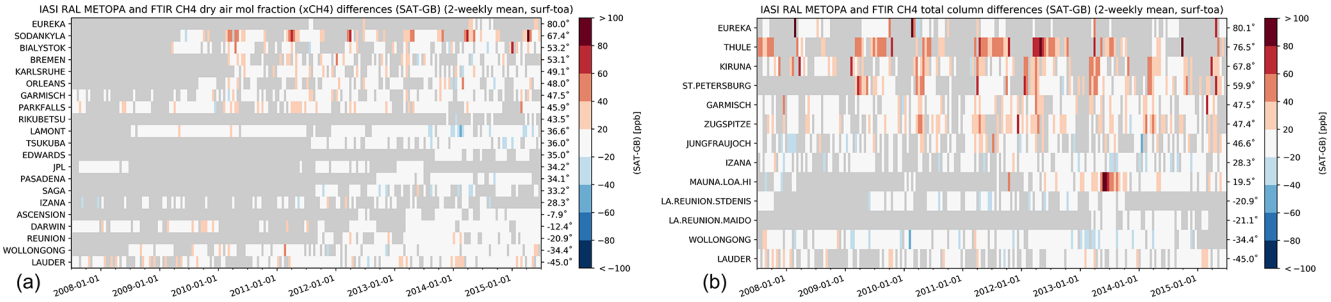


**Figure 16.** Mosaic plot of 2-week absolute mean differences (SAT–GB) at ground-based FTIR sites for the column-averaged dry-air mole fractions $XCH_4$ between RAL (no discontinuity correction applied) and ground-based FTIR measurements (**a** TCCON; **b** NDACC). The FTIR sites are sorted by their latitudes from north to south.

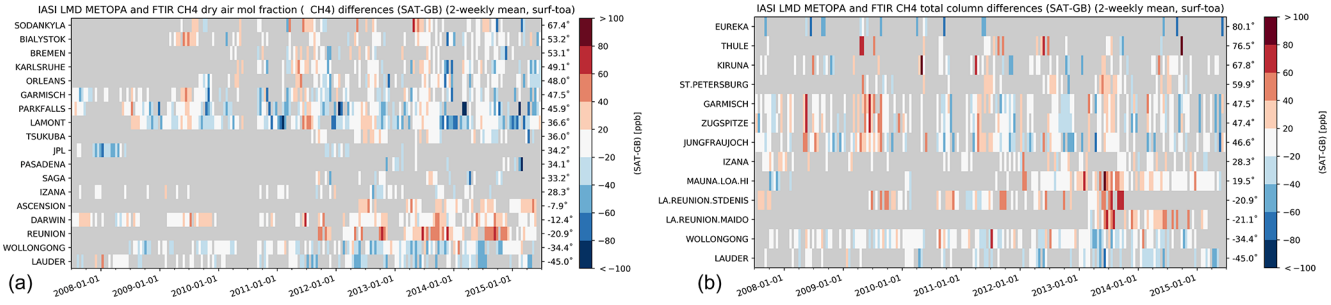


**Figure 17.** Same as Fig. 16 but for $mtCH_4$ from LMD and ground-based FTIR measurements.

**Table 6.** The mean station bias and mean station SD of the difference between IASI satellite $CH_4$ and ground-based FTIR measurements (SAT–GB).

| Satellite | LMD | | RAL | |
|---|---|---|---|---|
| | Mean | SD | Mean | SD |
| TCCON | −4.76 ppb | 24.00 ppb | 5.05 ppb | 11.23 ppb |
| NDACC | 1.83 ppb | 26.46 ppb | 9.79 ppb | 15.26 ppb |

itude, with strong positive values in the tropical (Ascension Island, Darwin, and Réunion) regions but negative values in the mid-latitude region. The bias at high-latitudes tends to be neutral to lightly positive. Moreover, there is a strong seasonal variation in the difference. For example, at Lamont, the LMD IASI is about 20 ppb larger than the TCCON measurement in summer, but it is about 60 ppb less than the TCCON measurement in winter. The mean and SD of the differences between LMD and NDACC measurements are 2.83 and 18.54 ppb, respectively. Similar to the TCCON measurements, the dependencies of the differences on latitude and time are also observed in comparison with the NDACC measurements.

A summary of the LMD and RAL comparison results with ground-based remote-sensing FTIR measurements is given in Table 6.

### 6.2.3 RAL trend and seasonal cycle

The seasonal variations and long-term trends of $XCH_4$ observed by co-located anomaly-corrected RAL and TCCON measurements are shown in Fig. 18. The $XCH_4$ trends derived from RAL are systematically lower than those derived from TCCON measurements at almost all sites. The mean $XCH_4$ annual growth rates, using only stations that cover a substantially long time window, are 4.84 ppb $yr^{-1}$, derived from the RAL measurements, and 6.1 ppb $yr^{-1}$, derived from TCCON measurements. Note that, due to the limited co-located RAL and TCCON measurements at Eureka, Rikubetsu, and Edwards (Fig. 16), the uncertainties in the trends at these sites are relatively large. In general, both the phase and amplitudes of the seasonal variations in $XCH_4$ observed by RAL and TCCON are close to each other. Again, looking at the long-running core stations, the RAL–TCCON long-term trend bias difference, ranging between $-2.72 \pm 0.62$ ppb $yr^{-1}$ (Lamont) and $-0.47 \pm 0.46$ ppb $yr^{-1}$ (Lauder), shows little latitudinal dependence, apart from the observation that Southern Hemisphere RAL–TCCON trend differences are slightly smaller, compared to those observed at Northern Hemisphere stations.

The seasonal variations and long-term trends of $XCH_4$ observed by RAL and NDACC measurements are shown in Fig. 19. Here the differences in the long-term trend biases show more station-to-station variability compared to TCCON. This is no doubt in part because NDACC also re-

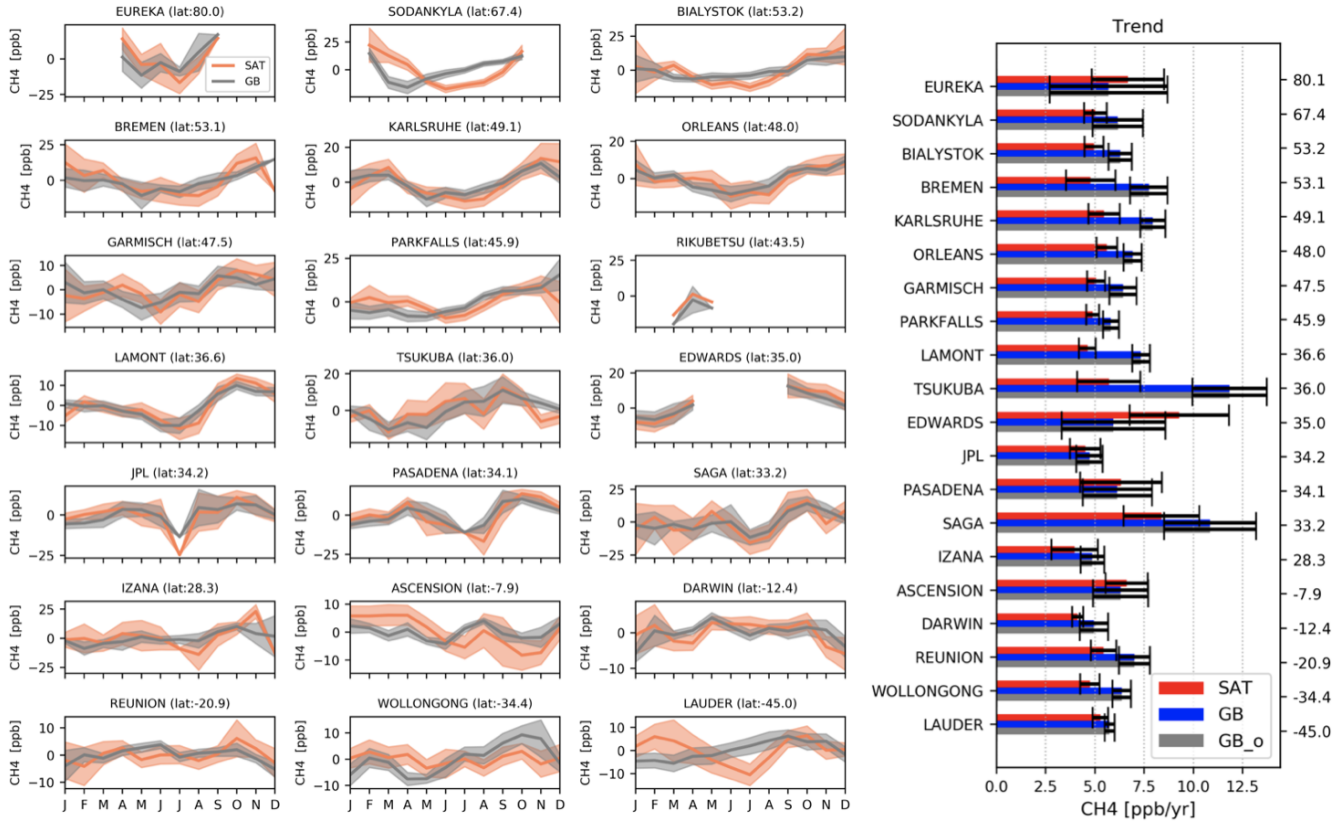


**Figure 18.** Left panels: the seasonal variations in $XCH_4$ observed by RAL (SAT) and smoothed TCCON (GB) measurements at each site. A +6.7 ppb discontinuity correction has been applied to the RAL data. Right panel: the $XCH_4$ annual growths derived from (discontinuity-corrected) RAL observations (SAT), TCCON measurements after smoothing (GB), and original TCCON measurements (GB_o). The latitude of the TCCON site is also remarked in the title or on the *y* axis. Not enough Rikubetsu data pairs (only eight) were available to calculate a long-term trend.

trieves (limited) profile information but also because harmonization within TCCON is more rigorous. Only Wollongong and Saint-Denis (Réunion) underestimate the long-term trend with respect to NDACC with (slightly) more than 2 ppb. All other stations feature positive and negative biases within this 2 ppb range. One could discern a small latitudinal dependence, with Southern Hemisphere stations featuring on average slightly stronger negative RAL–NDACC trend biases, but if it is present, it is very small. Note that the inverse dependence is shown in the TCCON comparisons ($\sim$ 1 ppb stronger negative RAL–TCCON biases in the Northern Hemisphere).

The strongest difference is observed at the Maïdo station, but here the uncertainty in the trends are very high since it only commenced measurements in 2013. The mean of the $XCH_4$ trends derived from the RAL data is 4.77 ppb yr$^{-1}$, which is only slightly less than that from NDACC measurements of 4.91 ppb yr$^{-1}$. The phases and amplitudes of the seasonal variations in $XCH_4$ observed by RAL and NDACC are similar at most sites, which is consistent with the TCCON measurements.

Of course, the long-term trend analysis is impacted by the 16 May 2013 discontinuity, and while we have applied a correction (+6.7 ppb shift) to the data, our analysis in Sect. 5.2 also showed that this corrected trend still ended up being $\sim$ 1 ppb yr$^{-1}$ lower compared to an approach where the dataset was split in two independent sections. However, regardless of the correction method used, RAL trends consistently (with little latitudinal dependence) underestimated the long-term trend when compared to CAMS (see Fig. 12), which is consistent with our TCCON comparisons (average RAL–TCCON trend difference of $-1.85 \pm 0.85$ ppb yr$^{-1}$). For NDACC, we see both over- and under-estimations of the trend, depending on the station, with on average a $-0.14 \pm 1.24$ ppb yr$^{-1}$ RAL–NDACC long-term trend difference.

### 6.2.4 LMD trend and seasonal cycle

The seasonal variations and long-term trends of $mtCH_4$ observed by LMD and TCCON measurements are shown in Fig. 20. When regarding the core stations, the LMD–TCCON trend difference ranges between $-4.48 \pm 1.41$ ppb yr$^{-1}$

(Lauder) and $0.91 \pm 1.35$ ppb yr$^{-1}$ (Darwin). In the Northern Hemisphere alone, it ranges between $-3.76 \pm 1.71$ ppb yr$^{-1}$ (Białystok) and $-1.09 \pm 1.65$ ppb yr$^{-1}$ (Orléans). Overall, the bias differences are more intense compared to the RAL–TCCON trend differences. We also typically find the strongest negative LMD–TCCON trend biases outside the 40° N–40° S range ($-4.48$ ppb yr$^{-1}$ at Lauder; $-3.76$ ppb yr$^{-1}$ at Sodankylä), but the variability within and outside the 40° N–40° S range is considerable. For instance, the trend difference at Orléans (48° N; $-1.09$ ppb yr$^{-1}$) is smaller than that observed at Lamont (36.6° N; $-2.36$ ppb yr$^{-1}$).

If we only consider LMD's core latitude region (30° N–30° S) (Izaña, Ascension Island, Darwin, and Réunion), the mean and SD of the $mtCH_4$ trends are $6.4 \pm 0.9$ ppb yr$^{-1}$, derived from TCCON measurements, and $6.0 \pm 1.8$ ppb yr$^{-1}$, derived from LMD measurements. Concerning the seasonal variation in the $mtCH_4$, the differences between the LMD and TCCON measurements are obvious at Białystok, Karlsruhe, Garmisch (European sites), Park Falls, Lamont (North American sites), Réunion, and Lauder. For example, at Park Falls, the $mtCH_4$ observed by LMD is high in July and low in January, but the $mtCH_4$ observed by the TCCON measurement is low in July and high in January. Moreover, the amplitude of the seasonal variation at Park Falls observed by LMD is about 80 ppb, which is 4 times larger than that observed by TCCON measurements of about 20 ppb. These differing seasonal patterns lead to the biases, as observed in Fig. 17 (LMD–TCCON and NDACC) and Fig. 6 (top row; LMD–CAMS), with significant negative biases in autumn–winter and positive biases in summer over the United States and (less intense) Europe.

The seasonal variations and long-term trends of $mtCH_4$ observed by LMD and NDACC measurements are shown in Fig. 21. Compared to our TCCON analysis, the station-to-station variability in the LMD–NDACC trend differences are substantially greater, ranging from $-5.35 \pm 3.09$ ppb yr$^{-1}$ (Eureka, Canada; 80.1° N) to $5.98 \pm 3.11$ ppb yr$^{-1}$ (Saint-Denis, Réunion (France), 20.9° S). St Petersburg (Russia) aside, one would see a very clear latitudinal dependence with LMD underestimating the long-term trend at high latitudes and overestimating them near the (sub)tropics. Note that in our analysis of the long-term trend using CAMS data (see Sect. 5.2 and Fig. 12), we saw a stable but slightly underestimated long-term trend in the (sub)tropics (roughly between 40° N and 40° S), with a rapidly increasing underestimation at higher latitudes.

The seasonal variations in $mtCH_4$ observed by LMD and NDACC are similar at Kiruna, Izaña, Mauna Loa, and Wollongong. However, the seasonal variations in $mtCH_4$ observed by LMD and NDACC are different at Garmisch, Zugspitze, Jungfraujoch (European sites), and Réunion. Both TCCON and NDACC measurements suggest that there is large uncertainty in the seasonal variation in $mtCH_4$ observed by LMD in Europe and Réunion.

Table 7 below shows the averaged (over all core stations) long-term trends of both LMD and (bias-corrected) RAL and their corresponding co-located NDACC and TCCON $mtCH_4$ time series. Overall, on average, both LMD and RAL underestimate the long-term trend. Also immediately apparent is the far greater standard deviation on the trend for LMD, compared to RAL, indicating stronger station-to-station variability.

### 6.3 Short summary

Of the three in situ measurement data used, AirCore, which measures profiles well into the stratosphere, can be considered the most representative. Unfortunately, while the LMD–AirCore bias is lower than that of RAL, its very limited dataset does not warrant a definitive conclusion with respect to the observed bias differences in the direct comparisons. This is certainly the case in view of the rather significant impact of, and the uncertainty associated with, the 16 May correction (RAL–AirCore bias from $-10.2$ to $-5.9$ ppb after correction).

Looking closer at the HIPPO measurements, we see that the biases with respect to HIPPO are far more intense in the LMD data compared to RAL. However, we do not see ever more negative LMD–HIPPO biases when moving towards the polar regions (as hinted at in Fig. 12); instead, we the strongest negative biases occurring around 40–50° N. Note that HIPPO measurements are concentrated around the Pacific Ocean area (Fig. 1) only and thus do not yield a global picture of the quality. However, they do cover a wide range of latitudes and cover (although not in the same year) all seasons. Looking at the region in more detail, we observe that the stronger bias outliers in Fig. 14 spatially (looking at the Pacific Ocean latitude band) and temporally (looking at the season) correspond closely with the areas that exhibit stronger biases in the CAMS–LMD comparisons (Fig. 6; top row). For instance, between 40 and 50° N, we see many strong negative LMD–HIPPO biases that correspond with the often observed stark negative LMD–CAMS bias over this area, particularly in October–January. On the other hand, around 30° S, LMD–CAMS often features strong positive biases, again corresponding with the values found in the LMD–HIPPO comparisons.

RAL–CAMS biases (Fig. 6; second row) over the Pacific Ocean, on the other hand, are not as strong, which is again reflected in the HIPPO comparisons. The IAGOS measurements, due to their irregular and often limited spatial and temporal distribution combined with inherent scatter did not allow us to determine whether the observed RAL–LMD differences (Fig. 6; bottom row) can be attributed to either algorithm. It is also very important to note that both HIPPO and IAGOS need an extension of the aircraft in situ profiles with CAMS model data. In particular, potential model errors in the exact location of the sharp $CH_4$ concentration that decrease as one ascends through the upper troposphere–lower

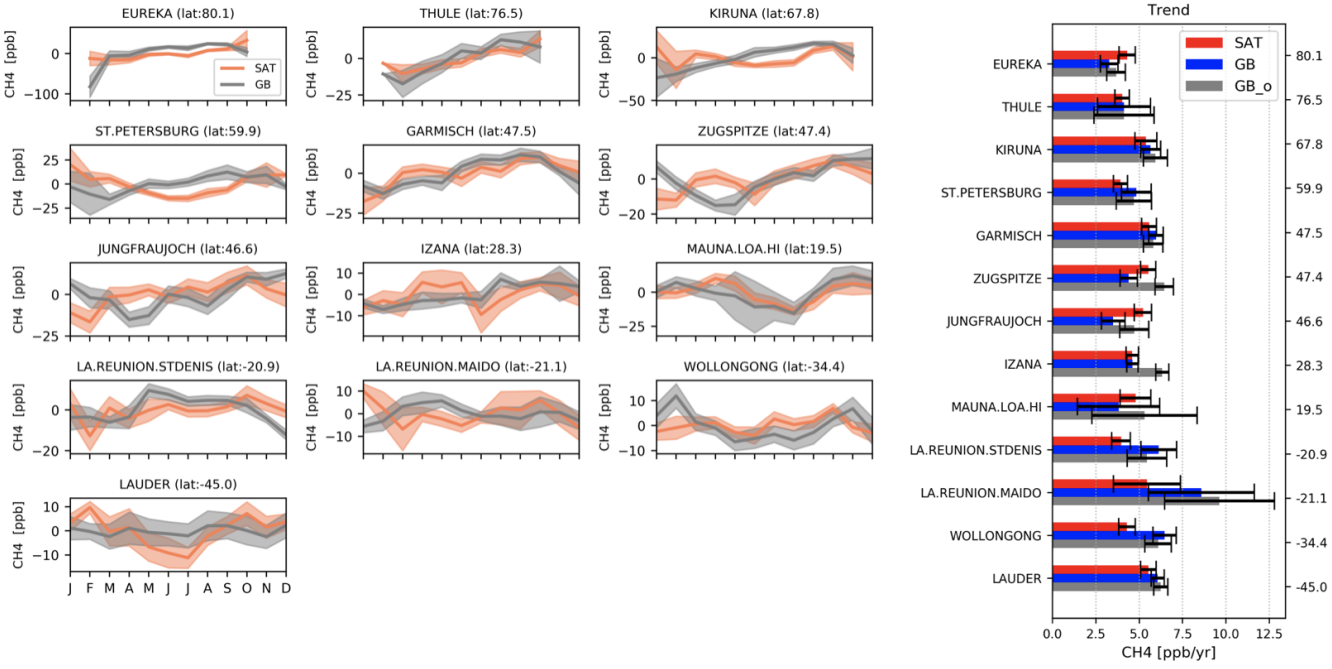


**Figure 19.** Same as Fig. 18 but for RAL and NDACC measurements.

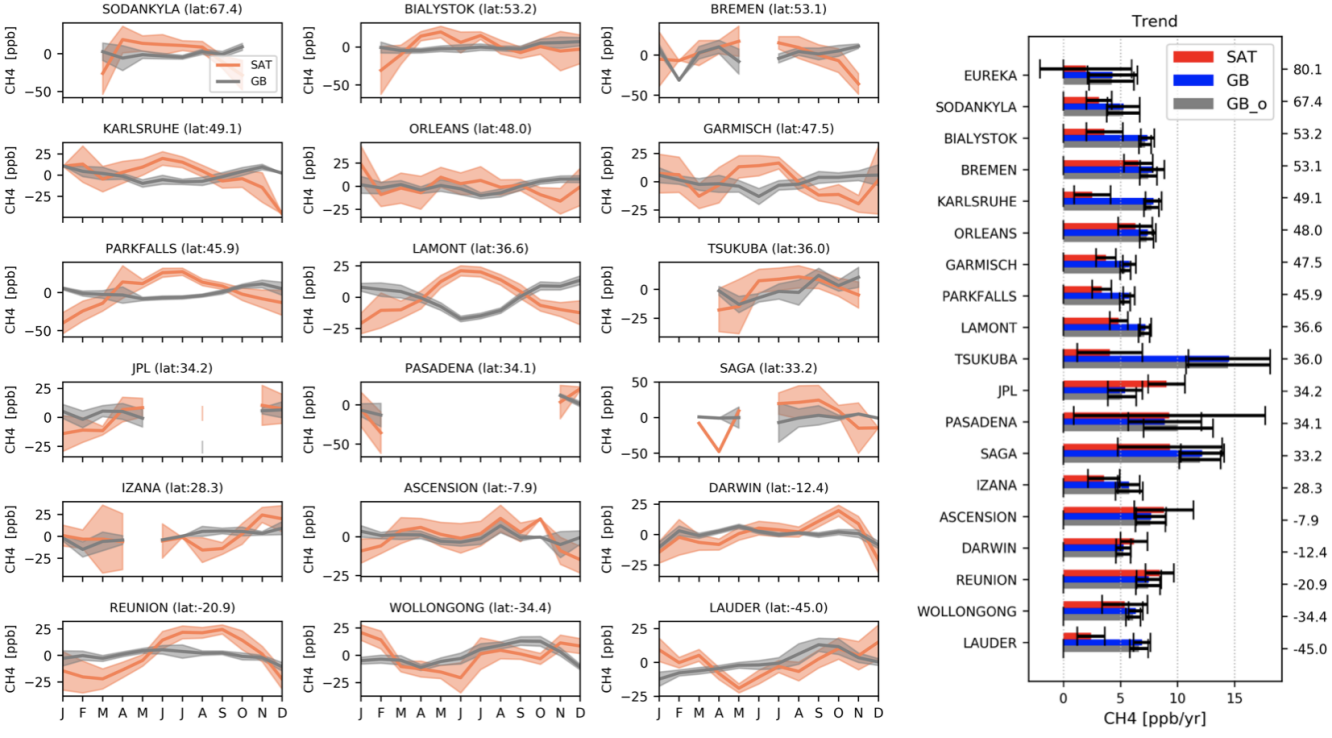


**Figure 20.** Same as Fig. 18 but for LMD and TCCON measurements.

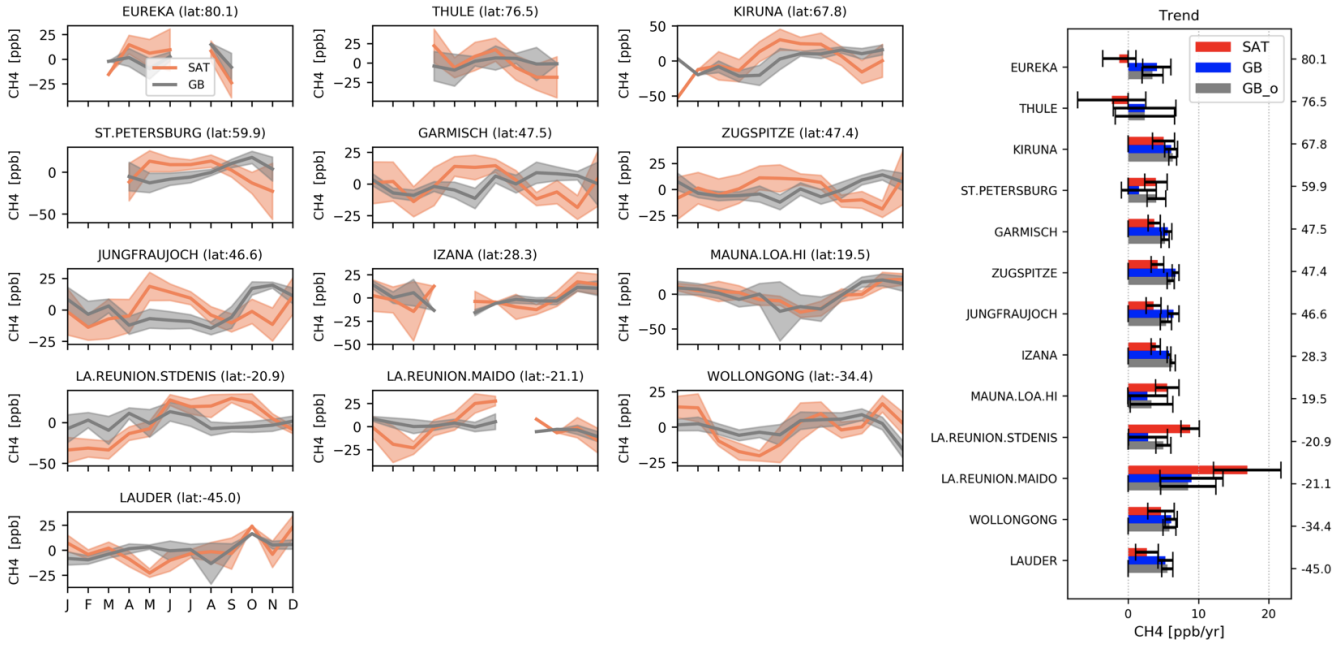


**Figure 21.** Same as Fig. 18 but for LMD and NDACC measurements.

**Table 7.** Mean and standard deviation of averaged (over long-running stations only) long-term trends differences (in ppb $yr^{-1}$) between IASI satellite and ground-based FTIR $CH_4$ measurements (SAT–GB). RAL measurements have been corrected for the discontinuity issue using a +6.7 ppb bias correction.

| Satellite | LMD | | GB | | RAL | | GB | |
|---|---|---|---|---|---|---|---|---|
| | Mean | SD | Mean | SD | Mean | SD | Mean | SD |
| TCCON | 4.26 | 1.27 | 6.31 | 0.81 | 4.84 | 0.47 | 6.10 | 0.74 |
| NDACC | 3.53 | 2.81 | 4.64 | 1.76 | 4.77 | 0.63 | 4.91 | 1.07 |

stratosphere (UTLS) can have a significant impact which is hard to quantify with no exact information on the true state of the atmosphere. Therefore, HIPPO's apparent corroboration of the satellite–CAMS comparison results should be interpreted with extreme caution. As a test, we artificially lowered or heightened the point at which the UTLS $CH_4$–CAMS transition kicks in by 100 hPa. This nullified most but not all of the strongest biases between LMD and HIPPO. Of course, this would imply that the direction of the hypothetical correction needs to change in sync with the latitudinal pattern in Fig. 14 as it features positive and negative biases alike.

The ground-based FTIR (TCCON and NDACC) measurements are used to compare with two IASI $CH_4$ products of RAL and LMD (Tables 6 and 7). The TCCON and NDACC measurements show that the systematic uncertainties in RAL and LMD data are both within ±10 ppb. However, the SD of the differences between LMD and FTIR is about 25 ppb, which is larger than that between RAL and FTIR (about 11–16 ppb). While the limited number of stations, the uncertainty in the individual station biases, and the considerable station-to-station variability make it impossible to definitively prove a strong latitudinal dependence of LMD's long-term trend, the comparisons with TCCON and NDACC certainly do not run contrary to our LMD–CAMS analysis in Sect. 5.2. The fact that the RAL–TCCON and RAL–NDACC trends do not feature such a latitudinal dependence further corroborates our analysis. We also observe significant differences at several sites with respect to the seasonal cycle in both TCCON and NDACC.

Here we need to add that there are very few stations within the 30° N–30° S latitude band at which the LMD algorithm was initially targeted. Also note that TCCON uses a profile-scaling retrieval approach in which the shape of the a priori profile cannot be altered resulting in potential smoothing errors.

## 7 Discussions

### 7.1 Two partial columns derived from RAL

In Sect. 6.1, it is found that the RAL $XCH_4$ is about 16.5 ppb underestimated between 15° N and 15° S compared to HIPPO measurements, and the underestimation is mainly coming from the lower partial column (0–6 km). The DOFs of RAL indicate that, apart from the higher latitudes (> 60° north and south), two independent partial columns can be obtained from the retrieved profiles. Unfortunately, the reference dataset remains fairly limited with regards to accurately assessing partial column information. Not enough vertical profile information is available in the ground-based FTIR measurements. As for the in situ observations, they have limited spatiotemporal coverage.

However, our analysis of the RAL upper–lower partial column differences compared to CAMS's partial column differences (see Sect. 4.2) equally showed a pronounced RAL lower-layer $qCH_4$ underestimation in the Pacific Ocean between 15° N and 15° S that was 12.5 ppb less than the CAMS model. This is consistent with the comparison between RAL and HIPPO in this lower layer.

Apart from the uncertainties within the CAMS model, there might be many reasons for the observed partial column differences from the RAL retrieval, such as the uncertainty in the spectroscopy and meteorological parameters, which could potentially affect partial columns differently. In addition, optimal estimation retrievals rely on a fine balance between placing too much constraint on the retrieval, resulting in too little retrieval information being added to the a priori and thus lower degrees of freedom, on the one hand, and placing not enough constraint on the retrieval, which risks producing unrealistic retrieval results. The latter often presents itself most clearly in unrealistic vertical retrieval profiles. Other observations that indicate a large sensitivity on the measured radiances are the 7 to 8 ppb bias between IFOV 1 and IFOV 3 of IASI and the stark contrast between the upper and lower partial column bias between adjacent land and sea measurements. If true, additional constraints need to be added to the retrieval, thereby adding stability at the cost of degrees of freedom, potentially losing the capacity to resolve two independent layers. Another factor that might be at play is the limited vertical resolution of the retrieved profile and the associated averaging kernel. Both partial columns effectively correspond with 1.5 layers in the profile, leaving little room for accurately capturing any potential variability in the sensitivity within each layer and ensuring no true independence between the partial columns. Further investigation is needed to understand the performance of the RAL two partial columns better when more in situ data become available.

### 7.2 LMD seasonal cycle discussion

By comparing LMD with RAL, CAMS, HIPPO, and ground-based FTIR measurements, it is found that the seasonal variation in $mtCH_4$ observed by LMD is different from others, especially in certain latitude regions (see Fig. 6). However, CAMS model data can hardly be regarded as the true state of the atmosphere; the data are only an approximation thereof. And while HIPPO measurements are highly accurate, they need to be expanded by model profiles to cover LMD's entire vertical sensitivity range. Changing the CAMS UTLS transition region resulted in significant changes in the observed biases with HIPPO. However, in most cases, the biases increased instead of decreased, and in the rare cases that the comparison improved, upward shifts of up to 4 km in the transition region were required. Ground-based remote-sensing TCCON FTIR measurements do not need model profile extensions, but they use a profile-scaling retrieval approach; since the shape of the profile is of great influence when applying LMD's sensitivity profile, one could certainly cast doubt on these observed biases as well. One can only point out that they confirm the HIPPO and CAMS observations – even though they use a different approach to construct their a priori profile shape. NDACC FTIR retrievals, on the other hand, use an optimal estimation approach which allows for profile shape optimization; here, again, we observe seasonal bias variability at, for instance, the Jungfraujoch data. Unfortunately, its vertical profile resolution is very limited (DOFs of about 2.5), and one could claim that this is insufficient for an accurate application of the LMD sensitivity profile. Therefore, in this section, we use the AirCore profiles at Boulder (39.7° N, 104.8° W) as the reference data to compare with the CAMS model and the LMD measurements. The AirCore profiles at Boulder are selected because the seasonal variations in $CH_4$ observed by LMD and RAL are very different at the North American temperate region (Fig. 10). There are five AirCore measurements available at Boulder between October 2017 and September 2019. Figure 22 shows the AirCore vertical profiles and the $mtCH_4$ derived from these AirCore profiles with the smoothing correcting using the LMD weighting function. The AirCore profile has a good vertical coverage, providing measurements between the surface and the stratosphere (about 25 km), so no (potentially flawed) model data are required to extend its profile over the troposphere–stratosphere boundary where a sharp decrease in $CH_4$ occurs. The seasonal variation in $mtCH_4$ derived from the LMD measurements within ±5° latitude and ±5° longitude around Boulder between June 2007 and June 2015 shows that $mtCH_4$ is high in summer and low in winter. However, the AirCore measurements show that the $mtCH_4$ is low in summer and high in autumn and winter, which is consistent with the TCCON measurements at Lamont (Fig. 20). The CAMS model at Boulder shows a seasonal cycle phase that is in line with the AirCore measurements, although its amplitude looks underestimated. Since we see a

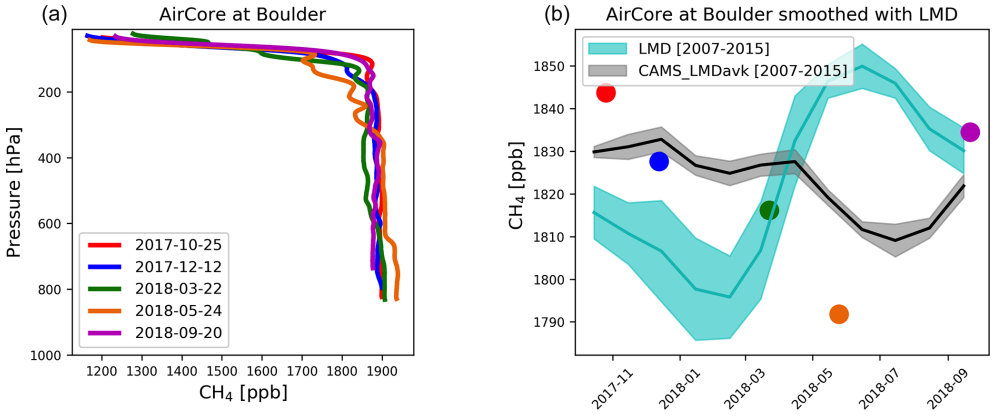


**Figure 22.** **(a)** The AirCore $CH_4$ profiles at Boulder between October 2017 and September 2018. **(b)** The time series of the mt$CH_4$ derived from the AirCore measurements with the smoothing correction using LMD weighting function, together with the mt$CH_4$ seasonal variation, derived from LMD measurements between July 2007 and June 2015 with a constant shift using the mean of the five AirCore measurements. CAMS_LMDavk corresponds with CAMS model data at Boulder smoothed by the LMD weighting function.

clear latitudinal dependence of both the long-term trend and the seasonal cycle offset, we have likewise obtained the long-term trend and seasonal cycles of the satellite–CAMS biases grouped per 10° latitude band. The results thereof are shown in Fig. 12. It shows that the amplitude of the seasonal cycle in the RAL–CAMS residuals is consistently lower than for LMD. Note that, as shown above, the CAMS seasonal cycle may itself not be accurate. However, what is of more interest is that we see a strong increase in the LMD residual seasonal amplitudes at higher ($> 50°$) latitudes. Likewise, for the long-term trend, RAL (both versions) shows little variability in the long-term trend of the RAL–CAMS residuals, whereas LMD shows a very strong decrease in the residual trend at latitudes exceeding (40°) in both hemispheres.

To conclude, while we accept that the used dataset is very limited, combined with all the other observations, AirCore measurements strongly suggest that the seasonal variation in mt$CH_4$ observed by LMD retrievals has a significant overestimation of the seasonal amplitude, together with a misrepresentation of the phase and an underestimation of the long-term trend above several higher-latitude regions. This observed decrease in fidelity at higher latitudes calls for an investigation of the robustness of LMD's neural network training database for these scenes. This is acknowledged by the algorithm development team as it currently advises users to be cautious when handling data from latitudes beyond 60° north and south. Our analysis, however, shows that, even at lower latitudes, time series start becoming less robust when compared to the 35° N–35° S latitude band.

## 8 Conclusions

The goal of this study was to perform an extensive validation of two IASI global $CH_4$ products (RAL and LMD), between July 2007 and June 2015, using a wide array of reference measurements.

The IASI products are compared to in situ and ground-based FTIR data. Average differences with respect to in situ measurements for LMD range between −0.3 and 10.9 ppb, while for RAL (discontinuity-corrected using a +6.7 bias shift) they range between −4.6 and −1.6 ppb. For the in situ comparisons, the differences from RAL are consistently more negative than those from LMD but in varying degrees. The SD of the observed differences are consistently smaller for RAL. For AirCore, these differences in SD are small (15.2 ppb for LMD vs. 14.1 ppb for RAL). For IAGOS and HIPPO, these differences are more substantial. Moreover, it is found that there is an underestimation of about 16.5 ppb in $XCH_4$ for RAL measurements in the tropics, which is mainly coming from the lower layer between 0 and 6 km. Using the ground-based FTIR sites as the reference data, the mean SD of the differences at the ground-based stations shows significantly lower values for RAL (11–16 ppb) than those for LMD (about 25 ppb). Looking at the latitudinal and seasonal variability at TCCON and NDACC sites, we observe that RAL shows little latitudinal dependence, while LMD data are on average larger than TCCON measurements in the tropical region and smaller than TCCON measurements at mid- and high-latitude sites.

An analysis of the long-term trend and seasonal cycles of the LMD and RAL products was carried out. We observed significant differences between the two algorithms. For RAL, we initially observed a significant underestimation of the long-term trend. This is due to an anomaly occurring on 16 May 2013 (due to a change in the IASI level 1 product) which caused a significant bias shift. The L1 discontinuity in May 2013 is expected to be resolved in a future updated version of the RAL $XCH_4$ product, using reprocessed L1 data. For LMD, we observed significant deviations (with respect

to RAL and the reference data) in the seasonal cycle (both in the magnitude of the amplitude and its phase) over several higher-latitude ($> 35°$) regions. We also found an underestimation of the long-term trend at higher latitudes. All in all, this results in large seasonal biases at these sites during the later years of the time series.

Users should also be aware that while the RAL partial columns manage to capture global features, they also still exhibit significant systematic errors. This observation, combined with the sensitivity of the retrieval with respect to the IASI L1 data and detector IFOV, also poses the question of whether the RAL optimal estimation retrieval requires more constraint. On the other hand, imposing a stronger prior constraint would result in more accurate retrieved values only if the "true" $CH_4$ distribution were adopted as the prior. Improvements to the scheme used to produce the data, which have been evaluated here, are ongoing and will be implemented for the next full reprocessing.

*Data availability.* The RAL data are publicly available at https://doi.org/10.5285/f717a8ea622f495397f4e76f777349d1 (Siddans et al., 2020). The LMD data are publicly available at https://iasi.aeris-data.fr/ (Crevoisier, 2023). The HIPPO data are publicly available at https://doi.org/10.3334/CDIAC/HIPPO_010 (Wofsy et al., 2017). The IAGOS data are publicly available at https://iagos.aeris-data.fr/download/ (Boulanger et al., 2020). The AirCore data are publicly available at https://doi.org/10.15138/6AV0-MY81 (Baier et al., 2021). The TCCON data are publicly available at https://tccondata.org/ (Total Carbon Column Observing Network, 2023; see Table 1 and references therein). The NDACC data are publicly available at https://ndacc.larc.nasa.gov/ (NDACC, 2024; see Table 2).

*Author contributions.* BD acted as the project's principal investigator. The validation work was carried out by BD, MZ, PP, and YK with support from BL, CCP, CS, and MDM. BK and RS provided RAL data and interacted with the validation team. MZ and BD prepared the paper. All authors contributed to the discussion and revision of the paper.

*Competing interests.* The contact author has declared that none of the authors has any competing interests.

*Disclaimer.* Note that neither the European Commission nor ECMWF is responsible for any use that may be made of the Copernicus information or data it contains.

Publisher's note: Copernicus Publications remains neutral with regard to jurisdictional claims made in the text, published maps, institutional affiliations, or any other geographical representation in this paper. While Copernicus Publications makes every effort to include appropriate place names, the final responsibility lies with the authors.

*Acknowledgements.* This work has been supported by the EUMETSAT independent validation of $CH_4$ products (grant no. ITT 18/205) project. Minqiang Zhou would like to thank the National Natural Science Foundation of China (grant no. 42205140) for additional support. The authors would like to thank all the teams that carried out the reference data measurements (TCCON, NDACC, IAGOS, HIPPO, and AirCore) and their respective funding agencies. CAMS model fields were generated using Copernicus Atmosphere Monitoring Service Information (2021).

*Financial support.* This research has been supported by the European Organization for the Exploitation of Meteorological Satellites (grant no. ITT 18/205) and the National Natural Science Foundation of China (grant no. 42205140).

*Review statement.* This paper was edited by Jian Xu and reviewed by two anonymous referees.

## References

Agusti-Panareda, A., Diamantakis, M., Bayona, V., Klappenbach, F., and Butz, A.: Improving the inter-hemispheric gradient of total column atmospheric $CO_2$ and $CH_4$ in simulations with the ECMWF semi-Lagrangian atmospheric global model, Geosci. Model Dev., 10, 1–18, https://doi.org/10.5194/gmd-10-1-2017, 2017.

Andersen, T., Scheeren, B., Peters, W., and Chen, H.: A UAV-based active AirCore system for measurements of greenhouse gases, Atmos. Meas. Tech., 11, 2683–2699, https://doi.org/10.5194/amt-11-2683-2018, 2018.

Baier, B., Sweeney, C., Tans, P., Newberger, T., Higgs, J., and Wolter, S.: NOAA AirCore atmospheric sampling system profiles (Version 20230831), NOAA GML [data set], https://doi.org/10.15138/6AV0-MY81, 2021.

Blumenstock, T., Hase, F., Schneider, M., García, O. E., and Sepúlveda, E.: TCCON data from Izana (ES), Release GGG2014.R1, CaltechDATA [data set], https://doi.org/10.14291/TCCON.GGG2014.IZANA01.R1, 2017.

Boulanger, D., Thouret, V., and Petzold, A.: IAGOS Data Portal, AERIS [data set], https://iagos.aeris-data.fr/download/ (last access: 12 January 2023), 2020.

Bruhwiler, L., Dlugokencky, E., Masarie, K., Ishizawa, M., Andrews, A., Miller, J., Sweeney, C., Tans, P., and Worthy, D.: CarbonTracker-$CH_4$: an assimilation system for estimating emissions of atmospheric methane, Atmos. Chem. Phys., 14, 8269–8293, https://doi.org/10.5194/acp-14-8269-2014, 2014.

Crevoisier, C.: Daily IASI/Metop-A LMD methane ($CH_4$) L2 product (mid-tropospheric column), version 8.3, IASI.AERIS Archive, https://iasi.aeris-data.fr/, last access: 12 January 2023.

Crevoisier, C., Nobileau, D., Fiore, A. M., Armante, R., Chédin, A., and Scott, N. A.: Tropospheric methane in the tropics – first year from IASI hyperspectral infrared observations, Atmos. Chem. Phys., 9, 6337–6350, https://doi.org/10.5194/acp-9-6337-2009, 2009.

Crevoisier, C., Nobileau, D., Armante, R., Crépeau, L., Machida, T., Sawa, Y., Matsueda, H., Schuck, T., Thonat, T., Pernin,

J., Scott, N. A., and Chédin, A.: The 2007–2011 evolution of tropical methane in the mid-troposphere as seen from space by MetOp-A/IASI, Atmos. Chem. Phys., 13, 4279–4289, https://doi.org/10.5194/acp-13-4279-2013, 2013.

De Mazière, M., Sha, M. K., Desmet, F., Hermans, C., Scolas, F., Kumps, N., Metzger, J.-M., Duflot, V., and Cammas, J.-P.: TCCON data from Réunion Island (RE), Release GGG2014.R11, CaltechDATA [data set], https://doi.org/10.14291/TCCON.GGG2014.REUNION01.R1, 2017.

De Mazière, M., Thompson, A. M., Kurylo, M. J., Wild, J. D., Bernhard, G., Blumenstock, T., Braathen, G. O., Hannigan, J. W., Lambert, J.-C., Leblanc, T., McGee, T. J., Nedoluha, G., Petropavlovskikh, I., Seckmeyer, G., Simon, P. C., Steinbrecht, W., and Strahan, S. E.: The Network for the Detection of Atmospheric Composition Change (NDACC): history, status and perspectives, Atmos. Chem. Phys., 18, 4935–4964, https://doi.org/10.5194/acp-18-4935-2018, 2018.

Deutscher, N. M., Notholt, J., Messerschmidt, J., Weinzierl, C., Warneke, T., Petri, C., and Grupe, P.: TCCON data from Bialystok (PL), Release GGG2014.R21, CaltechDATA [data set], https://doi.org/10.14291/TCCON.GGG2014.BIALYSTOK01.R2, 2019.

Dlugokencky, E. J., Steele, L. P., Lang, P. M., and Masarie, K. A.: The growth rate and distribution of atmospheric methane, J. Geophys. Res.-Atmos., 99, 17021–17043, https://doi.org/10.1029/94JD01245, 1994.

Edwards, P. G., Berutti, B., Blythe, P., Callies, J., Carlier, S., Fransen, C., Krutsch, R., Lefebvre, A.-R., Loiselet, M., and Stricker, N.: The MetOp satellite – Weather information from polar orbit, ESA Bulletin, 127, 8–17, 2006.

Feist, D. G., Arnold, S. G., John, N., and Geibel, M. C.: TCCON data from Ascension Island (SH), Release GGG2014.R01, CaltechDATA [data set], https://doi.org/10.14291/TCCON.GGG2014.ASCENSION01.R0/1149285, 2014.

Filges, A., Gerbig, C., Chen, H., Franke, H., Klaus, C., and Jordan, A.: The IAGOS-core greenhouse gas package: a measurement system for continuous airborne observations of $CO_2$, $CH_4$, $H_2O$ and CO, Tellus B, 67, 27989, https://doi.org/10.3402/tellusb.v67.27989, 2015.

Griffith, D. W., Deutscher, N. M., Velazco, V. A., Wennberg, P. O., Yavin, Y., Keppel-Aleks, G., Washenfelder, R. A., Toon, G. C., Blavier, J.-F., Paton-Walsh, C., Jones, N. B., Kettlewell, G. C., Connor, B. J., Macatangay, R. C., Roehl, C., Ryczek, M., Glowacki, J., Culgan, T., and Bryant, G. W.: TCCON data from Darwin (AU), Release GGG2014.R01, CaltechDATA [data set], https://doi.org/10.14291/TCCON.GGG2014.DARWIN01.R0/1149290, 2014a.

Griffith, D. W., Velazco, V. A., Deutscher, N. M., Paton-Walsh, C., Jones, N. B., Wilson, S. R., Macatangay, R. C., Kettlewell, G. C., Buchholz, R. R., and Riggenbach, M. O.: TCCON data from Wollongong (AU), Release GGG2014.R01, CaltechDATA [data set], https://doi.org/10.14291/TCCON.GGG2014.WOLLONGONG01.R0/1149291, 2014b.

Gurney, K. R., Law, R. M., Denning, A. S., Rayner, P. J., Baker, D., Bousquet, P., Bruhwiler, L., Chen, Y.-H., Ciais, P., Fan, S., Fung, I. Y., Gloor, M., Heimann, M., Higuchi, K., John, J., Maki, T., Maksyutov, S., Masarie, K., Peylin, P., Prather, M., Pak, B. C., Randerson, J., Sarmiento, J., Taguchi, S., Takahashi, T., and Yuen, C.-W.: Towards robust regional estimates of $CO_2$ sources and sinks using atmospheric transport models, Nature, 415, 626–630, https://doi.org/10.1038/415626a, 2002.

Hase, F., Hannigan, J., Coffey, M., Goldman, A., Höpfner, M., Jones, N., Rinsland, C., and Wood, S.: Intercomparison of retrieval codes used for the analysis of high-resolution, ground-based FTIR measurements, J. Quant. Spectrosc. Ra., 87, 25–52, https://doi.org/10.1016/j.jqsrt.2003.12.008, 2004.

Hase, F., Blumenstock, T., Dohe, S., Groß, J., and Kiel, M.: TCCON data from Karlsruhe (DE), Release GGG2014.R11, CaltechDATA [data set], https://doi.org/10.14291/TCCON.GGG2014.KARLSRUHE01.R1/1182416, 2015.

Inness, A., Ades, M., Agustí-Panareda, A., Barré, J., Benedictow, A., Blechschmidt, A.-M., Dominguez, J. J., Engelen, R., Eskes, H., Flemming, J., Huijnen, V., Jones, L., Kipling, Z., Massart, S., Parrington, M., Peuch, V.-H., Razinger, M., Remy, S., Schulz, M., and Suttie, M.: The CAMS reanalysis of atmospheric composition, Atmos. Chem. Phys., 19, 3515–3556, https://doi.org/10.5194/acp-19-3515-2019, 2019.

IPCC: Climate Change 2021: The Physical Science Basis. Contribution of Working Group I to the Sixth Assessment Report of the Intergovernmental Panel on Climate Change, edited by: Masson-Delmotte, V., Zhai, P., Pirani, A., Connors, S. L., Péan, C., Berger, S., Caud, N., Chen, Y., Goldfarb, L., Gomis, M. I., Huang, M., Leitzell, K., Lonnoy, E., Matthews, J. B. R., Maycock, T. K., Waterfield, T., Yelekçi, O., Yu, R., and Zhou, B., Cambridge University Press, Cambridge, United Kingdom and New York, NY, USA, 2391 pp. https://doi.org/10.1017/9781009157896, 2021.

Iraci, L. T., Podolske, J. R., Hillyard, P. W., Roehl, C., Wennberg, P. O., Blavier, J.-F., Landeros, J., Allen, N., Wunch, D., Zavaleta, J., Quigley, E., Osterman, G. B., Albertson, R., Dunwoody, K., and Boyden, H.: TCCON data from Edwards (US), Release GGG2014.R1, CaltechDATA [data set], https://doi.org/10.14291/TCCON.GGG2014.EDWARDS01.R1/1255068, 2016.

Karion, A., Sweeney, C., Tans, P., and Newberger, T.: AirCore: An innovative atmospheric sampling system, J. Atmos. Ocean. Tech., 27, 1839–1853, https://doi.org/10.1175/2010JTECHA1448.1, 2010.

Kawakami, S., Ohyama, H., Arai, K., Okumura, H., Taura, C., Fukamachi, T., and Sakashita, M.: TCCON data from Saga (JP), Release GGG2014.R0, CaltechDATA [data set], https://doi.org/10.14291/TCCON.GGG2014.SAGA01.R0/1149283, 2014.

Kirschke, S., Bousquet, P., Ciais, P., Saunois, M., Canadell, J. G., Dlugokencky, E. J., Bergamaschi, P., Bergmann, D., Blake, D. R., Bruhwiler, L., Cameron-Smith, P., Castaldi, S., Chevallier, F., Feng, L., Fraser, A., Heimann, M., Hodson, E. L., Houweling, S., Josse, B., Fraser, P. J., Krummel, P. B., Lamarque, J.-F., Langenfelds, R. L., Le Quéré, C., Naik, V., O'Doherty, S., Palmer, P. I., Pison, I., Plummer, D., Poulter, B., Prinn, R. G., Rigby, M., Ringeval, B., Santini, M., Schmidt, M., Shindell, D. T., Simpson, I. J., Spahni, R., Steele, L. P., Strode, S. A., Sudo, K., Szopa, S., van der Werf, G. R., Voulgarakis, A., van Weele, M., Weiss, R. F., Williams, J. E., and Zeng, G.: Three decades of global methane sources and sinks, Nat. Geosci., 6, 813–823, https://doi.org/10.1038/ngeo1955, 2013.

Kivi, R., Heikkinen, P., and Kyrö, E.: TCCON data from Sodankylä (FI), Release GGG2014.R0, CaltechDATA [data set], https://doi.org/10.14291/TCCON.GGG2014.SODANKYLA01.R0/1149280, 2014.

Knappett, D.: RAL IASI MetOp-A TIR Methane Dataset v2.0 Product User Guide, Documentation, Centre for Environmental Data Analysis (CEDA), https://doi.org/10.5281/zenodo.7357302, 2019.

Massart, S., Agusti-Panareda, A., Aben, I., Butz, A., Chevallier, F., Crevoisier, C., Engelen, R., Frankenberg, C., and Hasekamp, O.: Assimilation of atmospheric methane products into the MACC-II system: from SCIAMACHY to TANSO and IASI, Atmos. Chem. Phys., 14, 6139–6158, https://doi.org/10.5194/acp-14-6139-2014, 2014.

Morino, I., Matsuzaki, T., and Horikawa, M.: TCCON data from Tsukuba (JP), 125HR, Release GGG2014.R2, CaltechDATA [data set], https://doi.org/10.14291/TCCON.GGG2014.TSUKUBA02.R2, 2018a.

Morino, I., Yokozeki, N., Matsuzaki, T., and Horikawa, M.: TCCON data from Rikubetsu (JP), Release GGG2014.R2, CaltechDATA [data set], https://doi.org/10.14291/TCCON.GGG2014.RIKUBETSU01.R2, 2018b.

NDACC (Network for the Detection of Atmospheric Composition Change): Measurement Stations, https://ndacc.larc.nasa.gov/, last access: 12 January 2023.

Notholt, J., Petri, C., Warneke, T., Deutscher, N. M., Palm, M., Buschmann, M., Weinzierl, C., Macatangay, R. C., and Grupe, P.: TCCON data from Bremen (DE), Release GGG2014.R1, CaltechDATA [data set], https://doi.org/10.14291/TCCON.GGG2014.BREMEN01.R1, 2019.

Ostler, A., Sussmann, R., Rettinger, M., Deutscher, N. M., Dohe, S., Hase, F., Jones, N., Palm, M., and Sinnhuber, B.-M.: Multistation intercomparison of column-averaged methane from NDACC and TCCON: impact of dynamical variability, Atmos. Meas. Tech., 7, 4081–4101, https://doi.org/10.5194/amt-7-4081-2014, 2014.

Palmer, P. I., O'Doherty, S., Allen, G., Bower, K., Bösch, H., Chipperfield, M. P., Connors, S., Dhomse, S., Feng, L., Finch, D. P., Gallagher, M. W., Gloor, E., Gonzi, S., Harris, N. R. P., Helfter, C., Humpage, N., Kerridge, B., Knappett, D., Jones, R. L., Le Breton, M., Lunt, M. F., Manning, A. J., Matthiesen, S., Muller, J. B. A., Mullinger, N., Nemitz, E., O'Shea, S., Parker, R. J., Percival, C. J., Pitt, J., Riddick, S. N., Rigby, M., Sembhi, H., Siddans, R., Skelton, R. L., Smith, P., Sonderfeld, H., Stanley, K., Stavert, A. R., Wenger, A., White, E., Wilson, C., and Young, D.: A measurement-based verification framework for UK greenhouse gas emissions: an overview of the Greenhouse gAs Uk and Global Emissions (GAUGE) project, Atmos. Chem. Phys., 18, 11753–11777, https://doi.org/10.5194/acp-18-11753-2018, 2018.

Ramonet, M., Langerock, B., Warneke, T., and Eskes, H. J.: Validation report of the CAMS greenhouse gas global reanalysis, years 2003–2016, Copernicus Atmosphere Monitoring Service (CAMS) report, CAMS, https://doi.org/10.24380/y034-7672, 2020.

Rigby, M., Prinn, R. G., Fraser, P. J., Simmonds, P. G., Langenfelds, R. L., Huang, J., Cunnold, D. M., Steele, L. P., Krummel, P. B., Weiss, R. F., O'Doherty, S., Salameh, P. K., Wang, H. J., Harth, C. M., Mühle, J., and Porter, L. W.: Renewed growth of atmospheric methane, Geophys. Res. Lett., 35, L22805, https://doi.org/10.1029/2008GL036037, 2008.

Rigby, M., Montzka, S. A., Prinn, R. G., White, J. W. C., Young, D., O'Doherty, S., Lunt, M. F., Ganesan, A. L., Manning, A. J., Simmonds, P. G., Salameh, P. K., Harth, C. M., Mühle, J., Weiss, R. F., Fraser, P. J., Steele, L. P., Krummel, P. B., McCulloch, A., and Park, S.: Role of atmospheric oxidation in recent methane growth, P. Natl. Acad. Sci. USA, 114, 5373–5377, https://doi.org/10.1073/pnas.1616426114, 2017.

Rodgers, C. D.: Inverse Methods for Atmospheric Sounding – Theory and Practice, Series on Atmospheric Oceanic and Planetary Physics, vol. 2, World Scientific Publishing Co. Pte. Ltd, Singapore, https://doi.org/10.1142/9789812813718, 2000.

Rodgers, C. D. and Connor, B. J.: Intercomparison of remote sounding instruments, J. Geophys. Res., 108, 46–48, https://doi.org/10.1029/2002JD002299, 2003.

Schwietzke, S., Sherwood, O. A., Bruhwiler, L. M. P., Miller, J. B., Etiope, G., Dlugokencky, E. J., Michel, S. E., Arling, V. A., Vaughn, B. H., White, J. W. C., and Tans, P. P.: Upward revision of global fossil fuel methane emissions based on isotope database, Nature, 538, 88–91, https://doi.org/10.1038/nature19797, 2016.

Sherlock, V., Connor, B., Robinson, J., Shiona, H., Smale, D., and Pollard, D. F.: TCCON data from Lauder (NZ), 125HR, Release GGG2014.R0, CaltechDATA [data set], https://doi.org/10.14291/TCCON.GGG2014.LAUDER02.R0/1149298, 2014.

Siddans, R., Knappett, D., Kerridge, B., Waterfall, A., Hurley, J., Latter, B., Boesch, H., and Parker, R.: Global height-resolved methane retrievals from the Infrared Atmospheric Sounding Interferometer (IASI) on MetOp, Atmos. Meas. Tech., 10, 4135–4164, https://doi.org/10.5194/amt-10-4135-2017, 2017.

Siddans, R., Knappett, D., Kerridge, B., Latter, B., and Waterfall, A.: STFC RAL methane retrievals from IASI on board MetOp-A, version 2.0, CEDA Archive [data set], https://doi.org/10.5285/f717a8ea622f495397f4e76f777349d1, 2020.

Strong, K., Roche, S., Franklin, J. E., Mendonca, J., Lutsch, E., Weaver, D., Fogal, P. F., Drummond, J. R., Batchelor, R., and Lindenmaier, R.: TCCON data from Eureka (CA), Release GGG2014.R3, CaltechDATA [data set], https://doi.org/10.14291/TCCON.GGG2014.EUREKA01.R3, 2019.

Sussmann, R. and Rettinger, M.: TCCON data from Garmisch (DE), Release GGG2014.R2, CaltechDATA [data set], https://doi.org/10.14291/TCCON.GGG2014.GARMISCH01.R2, 2018.

Total Carbon Column Observing Network (TCCON): https://tccondata.org/, last access: 12 January 2023.

Turner, A. J., Frankenberg, C., Wennberg, P. O., and Jacob, D. J.: Ambiguity in the causes for decadal trends in atmospheric methane and hydroxyl, P. Natl. Acad. Sci. USA, 114, 5367–5372, https://doi.org/10.1073/PNAS.1616020114, 2017.

Warneke, T., Messerschmidt, J., Notholt, J., Weinzierl, C., Deutscher, N. M., Petri, C., and Grupe, P.: TCCON data from Orléans (FR), Release GGG2014.R1, CaltechDATA [data set], https://doi.org/10.14291/TCCON.GGG2014.ORLEANS01.R1, 2019.

Wennberg, P. O., Wunch, D., Roehl, C. M., Blavier, J.-F., Toon, G. C., and Allen, N. T.: TCCON data from Caltech (US), Release GGG2014.R1, CaltechDATA [data set], https://doi.org/10.14291/TCCON.GGG2014.PASADENA01.R1/1182415, 2015.

Wennberg, P. O., Roehl, C. M., Blavier, J.-F., Wunch, D., and Allen, N. T.: TCCON data from Jet Propulsion Laboratory (US), 2011, Release GGG2014.R1, CaltechDATA [data set], https://doi.org/10.14291/TCCON.GGG2014.JPL02.R1/1330096, 2016a.

Wennberg, P. O., Wunch, D., Roehl, C. M., Blavier, J.-F., Toon, G. C., and Allen, N. T.: TCCON data from Lamont (US), Release GGG2014.R1, CaltechDATA [data set], https://doi.org/10.14291/TCCON.GGG2014.LAMONT01.R1/1255070, 2016b.

Wennberg, P. O., Roehl, C. M., Wunch, D., Toon, G. C., Blavier, J.-F., Washenfelder, R., Keppel-Aleks, G., Allen, N. T., and Ayers, J.: TCCON data from Park Falls (US), Release GGG2014.R1, CaltechDATA [data set], https://doi.org/10.14291/TCCON.GGG2014.PARKFALLS01.R1, 2017.

WMO: WMO Greenhouse Gas Bulletin – World Meteorological Organization, WMO Bull., ISSN 2078-0796, 2017.

Wofsy, S. C.: HIAPER Pole-to-Pole Observations (HIPPO): fine-grained, global-scale measurements of climatically important atmospheric gases and aerosols, Philos. T. Roy. Soc. A, 369, 2073–2086, https://doi.org/10.1098/rsta.2010.0313, 2011.

Wofsy, S., Daube, B., Jimenez, R., Kort, E., Pittman, J., Park, S., Commane, R., Xiang, B., Santoni, G., Jacob, D., Fisher, J., Pickett-Heaps, C., Wang, H., Wecht, K., Wang, Q., Stephens, B., Shertz, S., Watt, A., Romashkin, P., Campos, T., Haggerty, J., Cooper, W., Rogers, D., Beaton, S., Hendershot, R., Elkins, J., Fahey, D., Gao, R., Schwarz, J., Moore, F., Montzka, S., Perring, A., Hurst, D., Miller, B., Sweeney, C., Oltmans, S., Hintsa, E., Nance, D., Dutton, G., Watts, L., Spackman, J., Rosenlof, K., Ray, E., Hall, B., Zondlo, M., Diao, M., Keeling, R., Bent, J., Atlas, E., Lueb, R. and Mahoney, M. J.: HIPPO Merged 10-Second Meteorology, Atmospheric Chemistry, and Aerosol Data, Version 1.0, UCAR/NCAR – Earth Observing Laboratory [data set], https://doi.org/10.3334/CDIAC/HIPPO_010, 2017.

Worden, J. R., Bloom, A. A., Pandey, S., Jiang, Z., Worden, H. M., Walker, T. W., Houweling, S., and Röckmann, T.: Reduced biomass burning emissions reconcile conflicting estimates of the post-2006 atmospheric methane budget, Nat. Commun., 8, 2227, https://doi.org/10.1038/s41467-017-02246-0, 2017.

Wunch, D., Toon, G. C., Wennberg, P. O., Wofsy, S. C., Stephens, B. B., Fischer, M. L., Uchino, O., Abshire, J. B., Bernath, P., Biraud, S. C., Blavier, J.-F. L., Boone, C., Bowman, K. P., Browell, E. V., Campos, T., Connor, B. J., Daube, B. C., Deutscher, N. M., Diao, M., Elkins, J. W., Gerbig, C., Gottlieb, E., Griffith, D. W. T., Hurst, D. F., Jiménez, R., Keppel-Aleks, G., Kort, E. A., Macatangay, R., Machida, T., Matsueda, H., Moore, F., Morino, I., Park, S., Robinson, J., Roehl, C. M., Sawa, Y., Sherlock, V., Sweeney, C., Tanaka, T., and Zondlo, M. A.: Calibration of the Total Carbon Column Observing Network using aircraft profile data, Atmos. Meas. Tech., 3, 1351–1362, https://doi.org/10.5194/amt-3-1351-2010, 2010.

Wunch, D., Toon, G. C., Blavier, J.-F. L., Washenfelder, R. A., Notholt, J., Connor, B. J., Griffith, D. W. T., Sherlock, V., and Wennberg, P. O.: The Total Carbon Column Observing Network, Philos. T. Roy. Soc. A, 369, 2087–2112, https://doi.org/10.1098/rsta.2010.0240, 2011.

Wunch, D., Toon, G. C., Sherlock, V., Deutscher, N. M., Liu, C., Feist, D. G., and Wennberg, P. O.: The Total Carbon Column Observing Network's GGG2014 Data Version, Tech. rep., California Institute of Technology, Pasadena, CA, https://doi.org/10.14291/tccon.ggg2014.documentation.R0/1221662, 2015.

Zhou, M., Langerock, B., Vigouroux, C., Sha, M. K., Ramonet, M., Delmotte, M., Mahieu, E., Bader, W., Hermans, C., Kumps, N., Metzger, J.-M., Duflot, V., Wang, Z., Palm, M., and De Mazière, M.: Atmospheric CO and $CH_4$ time series and seasonal variations on Reunion Island from ground-based in situ and FTIR (NDACC and TCCON) measurements, Atmos. Chem. Phys., 18, 13881–13901, https://doi.org/10.5194/acp-18-13881-2018, 2018.